The Astrophysical Journal, 666:290–308, 2007 September 1

GRAVITATIONAL COLLAPSE AND FRAGMENTATION OF MOLECULAR CLOUD CORES WITH GADGET-2

Guillermo Arreaga-García,[1] Jaime Klapp,[2] Leonardo Di G. Sigalotti,[3] and Ruslan Gabbasov[2]
Received 2006 October 20; accepted 2007 May 28

ABSTRACT

The collapse and fragmentation of molecular cloud cores is examined numerically with unprecedentedly high spatial resolutions, using the publicly released code GADGET-2. As templates for the model clouds we use the "standard isothermal test case" in the variant calculated by Burkert & Bodenheimer in 1993 and the centrally condensed, Gaussian cloud advanced by Boss in 1991. A barotropic equation of state is used to mimic the nonisothermal collapse. We investigate both the sensitivity of fragmentation to thermal retardation and the level of resolution needed by smoothed particle hydrodynamics (SPH) to achieve convergence to existing Jeans-resolved, finite-difference (FD) calculations. We find that working with 0.6–1.2 million particles, acceptably good convergence is achieved for the standard test model. In contrast, convergent results for the Gaussian-cloud model are achieved using from 5 to 10 million particles. If the isothermal collapse is prolonged to unrealistically high densities, the outcome of collapse for the Gaussian cloud is a central adiabatic core surrounded by dense trailing spiral arms, which in turn may fragment in the late evolution. If, on the other hand, the barotropic equation of state is adjusted to mimic the rise of temperature predicted by radiative transfer calculations, the outcome of collapse is a protostellar binary core. At least, during the early phases of collapse leading to formation of the first protostellar core, thermal retardation not only favors fragmentation but also results in an increased number of fragments, for the Gaussian cloud.

Subject headings: binaries: general — hydrodynamics — ISM: clouds — methods: numerical — stars: formation

1. INTRODUCTION

The high frequency of binaries among pre–main-sequence (Mathieu 1994; Ghez et al. 1997; Köhler & Leinert 1998; Köhler et al. 2000; Hubrig et al. 2001; Woitas et al. 2001; Brandeker et al. 2003; Boden et al. 2005) and main-sequence (Duquennoy & Mayor 1991; Fischer & Marcy 1992; Leinert et al. 1997; Patience et al. 1998; Cutispoto et al. 2002) stars of all ages, including the youngest, along with the incoming evidence for binary and low-order, multiple protostars (Looney et al. 1997, 2000; Terebey et al. 1998; Moriarty-Schieven et al. 2000; Reipurth et al. 2002; Anglada et al. 2004; Duchêne et al. 2004; Girart et al. 2004), points to fragmentation of molecular cloud cores as the most likely mechanism for explaining the majority of binary and multiple stars (Bodenheimer et al. 2000; Sigalotti & Klapp 2001a). In particular, a deep search for companions of embedded protostellar objects in Taurus and Ophiuchus by Duchêne et al. (2004) shows that binary and multiple protostars are a very frequent outcome of the fragmentation of prestellar cores and that their frequency and properties are not very sensitive to specific initial conditions. In this scenario, binary formation and star formation are contemporary processes that involve the gravitational collapse of cloud cores, from densities $\lesssim 10^{-19}$ g cm^{-3} and sizes of $\sim 10^{17}$ cm to final young stellar objects of densities $\gtrsim 10^{-1}$ g cm^{-3} and sizes of $\sim 10^{11}$ cm. The collapse of the core, or a portion of it, may then lead to fragmentation, which appears to be necessary to explain the wide range of observed distributions of mass ratios, periods, and orbital eccentricities of binary stars (Bodenheimer 1995). However, a direct conclusive proof of these assertions would certainly require a more continued detection of multiplicity among protostellar objects.

In general, the geometries involved in the process of star formation are complex, while the initial and boundary conditions are chaotic and poorly constrained by the observations. This explains why our present understanding of fragmentation is still mostly limited to three-dimensional (3D), numerical hydrodynamics calculations of the collapse of rotating gas clouds, starting from highly idealized geometries and initial conditions. Since the parameter space of initial conditions and constitutive physics is very large, the generality of the numerical results obtained is rather hard to establish. In addition, the outcome of fragmentation is highly sensitive to the details of the thermodynamics and radiation transfer effects that arise when the infalling gas becomes optically thick and switches from being approximately isothermal to being approximately adiabatic (Masunaga & Inutsuka 1999; Boss et al. 2000). Moreover, the dynamics of collapse depends also on a variety of thermal, chemical, and magnetic effects, with the result that the energy equation is not a local function of state. Therefore, proper numerical simulations of the protostellar collapse and fragmentation are difficult and demand very large computational resources that are not yet available.

Earlier work on protostellar collapse and fragmentation was largely based on low spatial resolution calculations of a uniform density, uniformly rotating, spherical gas cloud with an isothermal equation of state. As we shall see below, the bulk of these models suffered from an inherent numerical viscosity due to violation of the Jeans condition (Truelove et al. 1998), which caused artificial fragmentation to occur. Perhaps the most illustrative example of binary fragmentation during the isothermal collapse of an initially homogeneous cloud is given by the so-called "standard isothermal test case," first calculated by Boss & Bodenheimer (1979). Since then this model has acquired the status of a common

[1] Centro de Investigación en Física de la Universidad de Sonora, Apartado Postal 14740, CP 83000, Hermosillo, Sonora, Mexico.
[2] Instituto Nacional de Investigaciones Nucleares, ININ, Km. 36.5, Carretera México-Toluca, La Marquesa 52750, Estado de México, Mexico.
[3] Centro de Física, Instituto Venezolano de Investigaciones Científicas, IVIC, Apartado 21827, Caracas 1020A, Venezuela.

test calculation for convergence testing and intercode comparisons, with a fairly good agreement that the outcome of the first evolution is a protostellar binary system. In recent times, calculations of the standard isothermal test have focused on a slightly different set of initial conditions (Burkert & Bodenheimer 1993). This model and variants of it have been recalculated by several other authors, employing different numerical techniques and higher spatial resolution (Bate & Burkert 1997; Truelove et al. 1998; Klein et al. 1999; Boss et al. 2000; Kitsionas & Whitworth 2002; Springel 2005). All these authors predicted the formation of a binary system with the exception of Bate & Burkert (1997), who additionally found a bar between the binary fragments that broke up into a number of subfragments. Later on, Truelove et al. (1998) showed that fragmentation of the bar is a numerical artifact induced by violation of the Jeans condition. Recently, Springel (2005) performed a resolution study of the standard isothermal test case, using up to ~17.2 million particles, as part of the testing program for the smoothed particle hydrodynamics (SPH) component of the newly written code GADGET-2. However, his calculations were only followed over ~5.4 decades in density and terminated when the two forming blobs were just entering a phase of collapse upon themselves.

Although most fragmentation calculations apply to initially uniform conditions, it is clear from the observations that molecular cloud cores are centrally condensed (Ward-Thompson et al. 1994; André et al. 1998; Motte et al. 1998), with density profiles that are similar to those predicted by calculations of magnetized cores in the ambipolar diffusion stage (Basu & Mouschovias 1994; Ciolek & Mouschovias 1994; Mouschovias & Ciolek 1999). In response to this, a number of collapse models starting from centrally condensed, Gaussian density profiles have also been made. A particular computationally demanding isothermal, Gaussian cloud model was first calculated by Boss (1991), and thereafter recalculated by other authors as a further test case to check both the likelihood of fragmentation during the isothermal collapse phase and the reliability of the numerical code results (Burkert & Bodenheimer 1996; Truelove et al. 1997; Boss 1998; Boss et al. 2000; Sigalotti & Klapp 2001b, 2001c). Working at low spatial resolution, Boss (1991) predicted fragmentation into a quadruple system during the isothermal collapse of his Gaussian-cloud model. Similar results were also obtained by Burkert & Bodenheimer (1996), using higher spatial resolution. A new generation of three-dimensional collapse calculations started to appear later on with Truelove et al. (1997), who found that, working at a resolution higher than the local Jeans length, the effects of numerical viscosity are minimized preventing artificial fragmentation. In particular, the same Gaussian-cloud model of Boss (1991) did not fragment into a binary or quadruple system during the isothermal infall, but rather collapsed to form a singular filament consistent with the self-similar solution derived by Inutsuka & Miyama (1992) for the collapse of isothermal cylinders. Further highly resolved calculations (Boss et al. 2000; Sigalotti & Klapp 2001b, 2001c) have shown that adhering to the Jeans resolution condition not only changes the nature of the solution for the Gaussian-cloud model, but is the only road to guarantee convergence of the numerical solution. Other Jeans-resolved models starting from a Bonnor-Ebert sphere have been reported by Matsumoto & Hanawa (2003) and Hennebelle et al. (2004). In particular, the former authors performed a large survey of model parameters aimed at studying the effects of rotation speed, rotation law, and amplitude of the bar mode perturbation on fragmentation.

Clarification of the issue of fragmentation is of fundamental importance for explaining the duplicity of young stars and the coupling between the processes of binary and star formation. In connection with this, we note that the Gaussian-cloud model calculations of Boss (1998) suffered from artificial fragmentation despite obeying the Jeans condition, implying that it is a necessary but not sufficient condition for physically realistic fragmentation. On the other hand, Boss et al. (2000) demonstrated that the level of resolution that is needed in order to achieve reliable results may also depend on the particular numerical methods employed. In addition, thermal retardation due to nonisothermal heating may favor fragmentation during the collapse of the Gaussian cloud and prevent its runaway collapse toward an infinitely thin spindle (Boss et al. 2000). In order to investigate the actual level of resolution needed in an SPH-based code for achieving realistic fragmentation and convergence to existing Jeans-resolved, finite-difference (FD) calculations, we have recalculated the collapse of the standard isothermal test case, using the new parallel code GADGET-2 developed by Springel (2005). Since no definite solution has as yet been found for the nonisothermal collapse of the Gaussian cloud, here we also investigate the effects of thermal retardation on fragmentation, using a barotropic equation of state with unprecedentedly high spatial resolutions. In § 2 we add a few comments on the numerical methods. The initial conditions and details of the collapse models are given in § 3. This is followed, in § 4, by the presentation and discussion of the results and, in § 5, by the conclusions.

2. NUMERICAL METHODS

The calculations of this paper were performed using the parallel code GADGET-2, which is described in full by Springel (2005). The code is suitable for studying isolated, self-gravitating systems with unprecedentedly high spatial resolutions. So far, it has mainly been used in cosmological applications with several millions of particles. The code is based on the tree-PM method for computing the gravitational forces and on standard SPH methods for solving the 3D Euler equations of hydrodynamics. For a recent review on the theory and applications of SPH we refer the reader to Monaghan (2005).

As in most recent SPH codes used for problems involving gravitational fragmentation, GADGET-2 incorporates the following standard features: (1) The smoothing kernel $W_{ij} = W(|\boldsymbol{r}_i - \boldsymbol{r}_j|,\ h_i)$, where $|\boldsymbol{r}_i - \boldsymbol{r}_j|$ is the distance between two neighboring particles and h is the smoothing length, has compact support so that only a finite number of neighbors to each particle contribute to the SPH sums. In particular, the SPH sum for the density is

$$\rho_i = \sum_{j=1}^{N_{\rm neigh}} m_j W_{ij}, \tag{1}$$

where m_j denotes the mass of the jth particle and $N_{\rm neigh}$ is the number of neighbors. (2) Each particle i has its own smoothing length h_i, which evolves with time so that the mass contained in the kernel volume is a constant for the estimated density. For equal-mass particles, this is equivalent to demanding that the number of neighbors that contribute to the kernel be constant. As was recently demonstrated by Attwood et al. (2007), the fidelity of adaptive SPH calculations of self-gravitating systems relies on the requirement that $N_{\rm neigh}$ be kept exactly constant. This condition results in an effective reduction in the rates of numerical dissipation and diffusion. However, if the particles have unequal masses, as may be the case in centrally condensed configurations, GADGET-2 may incur a change in the number of neighbors at each time step. In this case, the problem is alleviated at the expense of using a large number ($N_{\rm tot}$) of particles. In particular, if $N_{\rm tot}/N_{\rm neigh}$ is increased, the timescales for numerical dissipation

and diffusion are extended and the reliability of the results is significantly improved (Attwood et al. 2007). For the present calculations, we choose $N_{\rm neigh} = 40 \pm \Delta N_{\rm neigh}$, where the tolerance $\Delta N_{\rm neigh} = 5$. For uniform density distributions, where all particles have the same mass, $\Delta N_{\rm neigh}$ is automatically set to zero, while for varying density distributions, where the mass of the particles may differ from one another, $N_{\rm neigh}$ may fluctuate between 35 and 45. In this case, the fidelity of the calculation can be recovered by employing large enough values of $N_{\rm tot}/N_{\rm neigh}$ to make the timescale of numerical dissipation come close to the evolution time. As we shall see in § 4, converging results for the Gaussian-cloud collapse are achieved for $N_{\rm tot} \gtrsim 5$ million particles, implying that $N_{\rm tot}/N_{\rm neigh}$ must at least be greater than $\sim 1.25 \times 10^5$. (3) In most SPH fragmentation calculations, particles are also allowed to have individual gravity softening lengths ϵ_i, which evolve in step with h_i so that the ratio $\epsilon_i(t)/h_i(t)$ is of order unity. In GADGET-2, ϵ is set equal to the minimum smoothing length $h_{\rm min}$, calculated over all particles at the end of each time step Δt. In this way, all particles share the same value of the gravity softening length, while the gravitational acceleration and the hydrostatic acceleration are still softened/smoothed on approximately the same scale. According to Bate & Burkert (1997), spurious fragmentation is avoided in SPH simulations when $\epsilon \approx h$. Also, they found that even with $\epsilon \approx h$, fragmentation is suppressed artificially in zones where the local Jeans mass is smaller than the minimum mass $M_{\rm min}$ that can be resolved so that sub-Jeans condensations are stabilized. These features were both independently confirmed by Whitworth (1998), using analytic means. (4) The gravitational forces are kernel-softened. In GADGET-2, the SPH sums are evaluated using the spherically symmetric M_4 kernel of Monaghan & Lattanzio (1985), and so gravity is spline-softened with this same kernel.

The positions and velocities of particles are advanced through a complete time step $\Delta t = t^{n+1} - t^n$ by means of a leapfrog integration scheme. In order to maintain hydrodynamic stability, the signal-velocity approach derived by Monaghan (1997) is used to calculate the Courant time step and the form of the artificial viscosity. In particular, for the Courant factor we choose $C_q = 0.1$. The strength of the artificial viscosity is regulated by setting the parameter $\alpha_{\rm visc} = 0.75$ in equation (14) of Springel (2005). These choices of the parameters are enough to produce accurate and stable results.

3. INITIAL CONDITIONS AND COLLAPSE MODELS

3.1. *The Uniform Cloud*

The collapse of the uniform cloud starts with initial conditions identical to the modified standard isothermal test case of Burkert & Bodenheimer (1993). The initial cloud is a perfect sphere of mass $M_0 = 1\ M_\odot$, radius $R = 4.99 \times 10^{16}$ cm ($\approx$0.016 pc), temperature $T = 10$ K, and constant density $\rho_0 = 3.82 \times 10^{-18}$ g cm^{-3}. The sphere is initially in solid-body rotation with angular velocity $\omega_0 = 7.2 \times 10^{-13}$ s^{-1}. The model has ideal gas thermodynamics with a mean molecular weight $\mu \approx 3$. These parameters correspond to initial ratios of the thermal and rotational energies to the absolute value of the gravitational energy of $\alpha \approx 0.26$ and $\beta \approx 0.16$, respectively. The isothermal sound speed of the gas is $c_{\rm iso} \approx 1.66 \times 10^4$ cm s^{-1}, and the initial mean free-fall time is $t_{\rm ff} \approx 1.07 \times 10^{12}$ s. In addition, a small-amplitude ($a = 0.1$), $m = 2$ density perturbation of the form

$$\rho = \rho_0[1 + a\cos(m\phi)] \tag{2}$$

is imposed on the underlying uniform density distribution, where ϕ is the azimuthal angle about the z-axis.

3.2. *The Gaussian Cloud*

The Gaussian cloud employs the same initial conditions advanced by Boss (1991) in his case C4. They correspond to a centrally condensed sphere of mass $M_0 = 1\ M_\odot$ and radius $R = 4.99 \times 10^{16}$ cm. The density distribution is exponentially falling from the center and is given by

$$\rho(r) = \rho_c \exp\left[-\left(\frac{r}{b}\right)^2\right], \tag{3}$$

where $\rho_c = 1.7 \times 10^{-17}$ g cm^{-3} is the initial central density and $b \approx 0.578R$ is a length chosen such that the central density is 20 times the density at the outer edge. The gas has a temperature of 10 K and a chemical composition of $X = 0.769$, $Y = 0.214$, and $Z = 0.017$, corresponding to a mean molecular weight $\mu \approx 2.28$. The cloud is given a 10% bar mode ($m = 2$) perturbation having the same form as expression (2). Solid-body rotation is assumed at the rate of $\omega_0 = 1.0 \times 10^{-12}$ s^{-1}. With this choice of the parameters, the values of α and β are the same as for the uniform model, while the isothermal sound speed is $c_{\rm iso} \approx 1.90 \times 10^4$ cm s^{-1} and the central free-fall time is $t_{\rm ff} \approx 5.10 \times 10^{11}$ s. Note that the Gaussian cloud has the same global properties as the uniform cloud in spite of being centrally condensed. A Gaussian cloud of this type is in fair agreement with observations of precollapse cloud cores, which indicate that their internal structure fits with radial density profiles that flatten out near the center, implying a finite central condensation (André et al. 1998; Motte et al. 1998). In addition, it does not have the extreme central condensation of the singular isothermal sphere ($\rho \propto r^{-2}$), which, if uniformly rotating, would presumably be stable against fragmentation (Tsai & Bertschinger 1989).

3.3. *Equation of State*

The isothermal phase of collapse is approximately valid for densities in the range of $\sim 10^{-19}$ to $\sim 10^{-13}$ g cm^{-3}. At higher densities the collapse of some portions of the cloud core becomes nonisothermal once the heating rate, due to gas compression, exceeds locally the cooling rate, due to dust grain radiation. As a result, the temperature increases in those portions. According to Masunaga & Inutsuka (1999), the point at which the collapse becomes nonisothermal is not necessarily determined by the point at which the core becomes optically thick to its own radiation, but rather by two other possible situations: (1) the cloud core starts heating up just before it becomes optically thick because the dust grains cease to be efficient coolants, or (2) it begins to heat up thereafter because radiative diffusion allows the core to remain isothermal. The former condition is a more likely scenario in regions where both the metallicity and temperature are lower, while the second one is more appropriate in regions with higher metallicity and higher temperature.

Precise knowledge of the dependence of temperature on density at the transition from isothermal to nonisothermal collapse will require solving the radiative transfer problem coupled to a fully self-consistent energy equation. Spherically symmetric calculations by Masunaga et al. (1998), using a nongray, variable Eddington factor method have shown that for typical star-forming conditions, heating prior to the gas becoming optically thick in the cloud center is modest (from 10 K to only about 13 K). In addition, nonisothermal collapse of the central cloud is expected to begin at densities $\gtrsim 10^{-15}$ g cm^{-3} (Inutsuka & Miyama 1997). On the other hand, the validity of these results in full three-space dimensions was studied by Boss et al. (2000) for the collapse of the Gaussian cloud, using nonisothermal thermodynamics and

solving the mean intensity equation in the Eddington approximation with detailed equations of state (see Boss & Myhill 1992). They found that the collapse remains strictly isothermal up to $\sim 10^{-16}$ g cm^{-3} (see Fig. 4 of Boss et al. 2000). At higher densities the collapse is near isothermal, with the temperature rising very slowly from 10 to $\sim$11.2 K by the time $\rho \sim 10^{-14}$ g cm^{-3}. Soon afterward, when $\rho \gtrsim 10^{-14}$ g cm^{-3}, the collapse becomes nonisothermal and the temperature rises steeply with the density. Boss et al. (2000) went on to argue that for the nonisothermal Gaussian cloud, the variation of temperature with density cannot be fit well with a single power law in density because the derived pressures used to update the momentum equations will differ between a calculation using a stiffened equation-of-state approximation and a fully consistent calculation incorporating radiative transfer.

A drawback of fully nonisothermal calculations is the severe computational burden imposed by solving the radiative transfer equations at high spatial resolution, even in the Eddington approximation. Therefore, many nonisothermal, 3D collapse calculations to date rely on a barotropic prescription for the thermodynamics. In this approximation, a self-consistent energy equation is not needed and the thermal properties of the gas are expressed solely in terms of the density. Here the uniform- and Gaussian-cloud models are calculated using the barotropic pressure-density relation (e.g., Boss et al. 2000)

$$p = c_{\rm iso}^2 \rho + K\rho^{\gamma}, \tag{4}$$

where $\gamma = 5/3$ is the adiabatic exponent in the optically thick regime and K is a constant set by the requirement that the isothermal and adiabatic parts of equation (4) are equal at some critical density $\rho = \rho_{\rm crit}$ separating the isothermal from the nonisothermal regimes, i.e.,

$$K = c_{\rm iso}^2 \rho_{\rm crit}^{1-\gamma}. \tag{5}$$

With the above prescriptions, the local sound speed becomes

$$c = c_{\rm iso}\left[1 + \left(\frac{\rho}{\rho_{\rm crit}}\right)^{\gamma-1}\right]^{1/2}, \tag{6}$$

so that $c \approx c_{\rm iso}$ when $\rho \ll \rho_{\rm crit}$ and $c \approx c_{\rm ad} = \gamma^{1/2} c_{\rm iso}$ when $\rho \gg \rho_{\rm crit}$. Since the present calculations apply only to the initial phase of fragmentation, we shall use equations (4)–(6) for temperatures well below 100 K. At such temperatures, a value of $\gamma = 5/3$ is appropriate because the rotational and vibrational degrees of freedom of molecular hydrogen are frozen out, and so only translational degrees of freedom need be considered (Winkler & Newman 1980; Boss et al. 2000).

The effects of thermal retardation on fragmentation are studied for two different choices of the free parameter $\rho_{\rm crit}$ (see Table 1). A value of $\rho_{\rm crit} = 5.0 \times 10^{-14}$ g cm^{-3} produces a behavior that is more representative of the near isothermal phase and fits better the Eddington approximation solution of Boss et al. (2000). Conversely, a value of $\rho_{\rm crit} = 5.0 \times 10^{-12}$ g cm^{-3} prolongs the isothermal phase of collapse to unrealistically high densities, but allows direct comparison with the fully isothermal, FD calculations of Burkert & Bodenheimer (1993, 1996) and the nonisothermal (barotropic), SPH calculations of Kitsionas & Whitworth (2002), who also used $\rho_{\rm crit} = 5.0 \times 10^{-12}$ g cm^{-3}.

TABLE 1
Collapse Models

Model	$\rho_{\rm crit}$ (g cm^{-3})	Number of Particles	Final Outcome	Convergence
Uniform Clouds				
U1A	5.0×10^{-12}	600,000	Binary	Yes
U2A	5.0×10^{-12}	1,200,000	Binary	Yes
U1B	5.0×10^{-14}	600,000	Binary	Yes
U2B	5.0×10^{-14}	1,200,000	Binary	Yes
Gaussian Clouds				
G1A	5.0×10^{-12}	600,000	Binary	No
G2A	5.0×10^{-12}	1,200,000	Triple	No
G3A	5.0×10^{-12}	2,000,000	Triple	No
G4A	5.0×10^{-12}	3,000,000	Binary	Partial
G5A	5.0×10^{-12}	5,000,000	Single	Yes
G6A	5.0×10^{-12}	10,000,000	Single	Yes
G1B	5.0×10^{-14}	600,000	Triple	No
G2B	5.0×10^{-14}	1,200,000	Triple	No
G3B	5.0×10^{-14}	2,000,000	Quadruple	No
G4B	5.0×10^{-14}	3,000,000	Binary	Partial
G5B	5.0×10^{-14}	5,000,000	Binary	Yes
G6B	5.0×10^{-14}	10,000,000	Binary	Yes

3.4. *The Jeans Condition*

After the work of Truelove et al. (1997), a new generation of collapse and fragmentation calculations began to appear because of the need of appropriate spatial resolution requirements. They demonstrated, using a FD Cartesian code based on an adaptive mesh refinement (AMR) technique, that perturbations arising from the FD discretization of the gravitohydrodynamics equations can induce artificial fragmentation in isothermal collapse calculations for which the Cartesian cell size Δx exceeds one-fourth of the local Jeans length

$$\lambda_{\rm J} = \left(\frac{\pi c_{\rm iso}^2}{\rho G}\right)^{1/2}, \tag{7}$$

where G is the gravitational constant. This is equivalent to claiming that the mass within a cell must never exceed 1/64 of the Jeans mass $\rho\lambda_{\rm J}^3$ in order to avoid artificial fragmentation. They also found that by fulfilling this condition, the isothermal Gaussian cloud did not fragment into a binary or quadruple system as in previous calculations (Boss 1991; Burkert & Bodenheimer 1996), but, rather, underwent runaway collapse to a singular filament. Convergence to this solution was subsequently confirmed by Boss et al. (2000) and Sigalotti & Klapp (2001b), using Jeans-resolved calculations of the same Gaussian cloud with the aid of independent adaptive, FD codes based on spherical coordinates.

The corresponding Jeans condition for SPH was derived by Bate & Burkert (1997), who found that true fragmentation is captured in SPH calculations provided that (1) the gravity softening and the particle smoothing lengths have similar scales (i.e., $\epsilon \approx h$), and (2) the minimum resolvable mass $M_{\rm min} \sim N_{\rm neigh} m$, where m is the mass of a single SPH particle, be less than the local Jeans mass

$$M_{\rm J} \sim \frac{6c^3}{G^{3/2}\rho^{1/2}}, \tag{8}$$

so that the Jeans condition can be written as an upper limit on the mass of a single SPH particle

$$m < \frac{6c^3}{N_{\rm neigh} G^{3/2}\rho^{1/2}}. \tag{9}$$

Whitworth (1998) derived analytically the Jeans criterion for a gas simulated using SPH methods in which $N_{\rm neigh}$ is held constant and $\epsilon = h$. He showed that artificial formation of condensations by numerical instability are effectively suppressed as long as $M_{\rm min} < M_{\rm J}$. Thus, only structures involving more mass than $M_{\rm min}$ are resolved properly. He also confirmed the findings of Bate & Burkert (1997) that even with $\epsilon \approx h$, fragmentation is suppressed artificially in regions where $M_{\rm J} < M_{\rm min}$, implying that unresolved Jeans-unstable condensations are stabilized numerically. These results were independently confirmed by Hubber et al. (2006) by means of a simple perturbation analysis, using the standard M_4 kernel and kernel-softening gravity options. They showed that SPH only captures genuine and resolved fragmentation and that failing to satisfy the Jeans condition simply suppresses true fragmentation, rather than promoting artificial fragmentation as with FD methods.

As shown in Table 1, we consider two sequences of model calculations. One sequence consists of four independent runs of the uniform-cloud test, while the other sequence is made up of 12 calculations of the Gaussian cloud. The models in both sequences differ only in the value of $\rho_{\rm crit}$ and in the total number of SPH particles from the outset. For example, in the uniform clouds all SPH particles have the same mass. With 600,000 particles (models U1A and U1B), the mass of a particle is $m \approx 1.67 \times 10^{-6}\ M_\odot$, while in the runs with 1.2 million particles (cases U2A and U2B), the mass of a particle is $m \approx 8.33 \times 10^{-7}\ M_\odot$. At $\rho = \rho_{\rm crit}$, equation (9) takes the form

$$m < \frac{6c_{\rm iso}^3}{N_{\rm neigh}\rho_{\rm crit}^{1/2}}\left(\frac{2}{G}\right)^{3/2}. \qquad (10)$$

For $\rho_{\rm crit} = 5 \times 10^{-12}$ g cm^{-3}, the right side of the above inequality gives $\approx 3.19 \times 10^{-5}\ M_\odot$, implying that for these two runs the Jeans condition is satisfied at the point where the collapse ceases to be isothermal. We compare the results of models U1A and U2A with those obtained by Kitsionas & Whitworth (2002), who also employed 600,000 SPH particles in one model calculation with no particle splitting. They followed the collapse to $\rho_{\rm max} \approx 3.0 \times 10^{-9}$ g cm^{-3}. At these densities, the right side of equation (9) gives $\approx 2.83 \times 10^{-4}\ M_\odot$. Similarly, models U1B and U2B are compared with the AMR calculations of Klein et al. (1999), who followed the evolution up to $\rho_{\rm max} \approx 1.08 \times 10^{-10}$ g cm^{-3}. At this density, the right side of equation (9) becomes $\approx 5.30 \times 10^{-3}\ M_\odot$. Thus, $M_{\rm J}$ increases deep into the nonisothermal collapse, making the Jeans condition less stringent than for the isothermal collapse. The collapse of the Gaussian cloud was recalculated with different resolutions, ranging from 0.6 to 10 million particles (see Table 1). While adhering to the Jeans condition, these models will allow us to find at which spatial resolution SPH would yield converging results for the nonisothermal collapse and fragmentation of the Gaussian cloud. As far as we know, there are no SPH calculations of the Gaussian cloud available in the literature, which also justifies the present study.

3.5. *Setup of the Initial Models*

In order to set up the initial particle distribution, we first define a Cartesian box with sides equal to twice a specified radius $R_b \gtrsim R = 4.99 \times 10^{16}$ cm, and with its geometrical center coinciding with the origin ($x = y = z = 0$) of a Cartesian coordinate system. The box is then subdivided into regular cubic cells of volume $\Delta^3 = \Delta x \Delta y \Delta z$ each. The spherical cloud is then copied within the box by placing an SPH particle at the center of each cell at distances $d \leq R$ from the origin, so that the region outside the sphere is a vacuum. A little amount of disorder is added to the regular distribution of particles by shifting each particle a distance $\Delta/4$ from its cell-center location and along a specified direction, which is chosen randomly among the three Cartesian axes. We define the mass of particle i at location (x_i, y_i, z_i) to be

$$m_i = \rho(x_i,\ y_i,\ z_i)\Delta^3, \qquad (11)$$

where $\rho(x_i,\ y_i,\ z_i)$ is either a constant, as for the uniform cloud, or given by equation (3), as for the Gaussian cloud. The initial averaged radial density profiles (*crosses*) for the uniform and Gaussian clouds are shown in Figure 1. The solid lines depict the corresponding exact profiles. The small scatters in the numerical profiles near the center and near the outer edge are only cosmetic because they are an effect of the disordered position of particles on the radial averaging procedure.

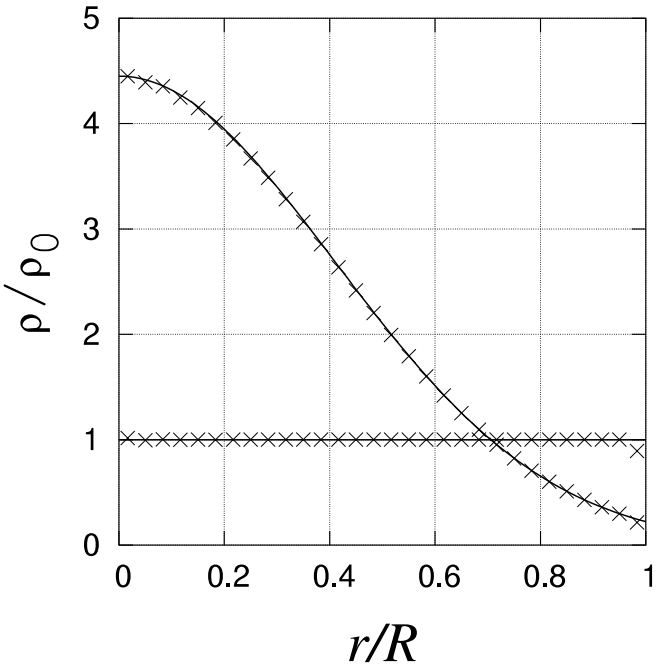

FIG. 1.—Averaged radial density profiles as calculated from the initial distribution of particles (*crosses*) for both the uniform- and Gaussian-cloud models with 600,000 SPH particles. The solid lines depict the corresponding exact profiles. The density is expressed in terms of the reference value $\rho_0 = 3.82 \times 10^{-18}$ g cm^{-3}, and the radial distance is given in terms of the initial cloud radius.

Solid-body rotation about the z-axis is assumed in a counterclockwise sense by assigning to particle i an initial velocity given by

$$\boldsymbol{v}_i = (\omega_0 x_i,\ -\omega_0 y_i,\ 0). \qquad (12)$$

Finally, the bar mode density perturbation given by equation (2) is applied by modifying the mass of particle i according to

$$m_i \rightarrow m_i[1 + a\cos(m\phi_i)], \qquad (13)$$

where ϕ_i denotes the azimuthal position of that particle. The Mezquite Cluster of the University of Sonora, equipped with 70 Dual Intel (64 bit) Xeon processors of 3.6 GHz each, was used for the parallel calculations of this paper.

4. RESULTS

4.1. *Collapse of the Uniform Cloud*

The collapse of the uniform cloud is a valuable fragmentation test to explore the convergence of the solution at resolutions

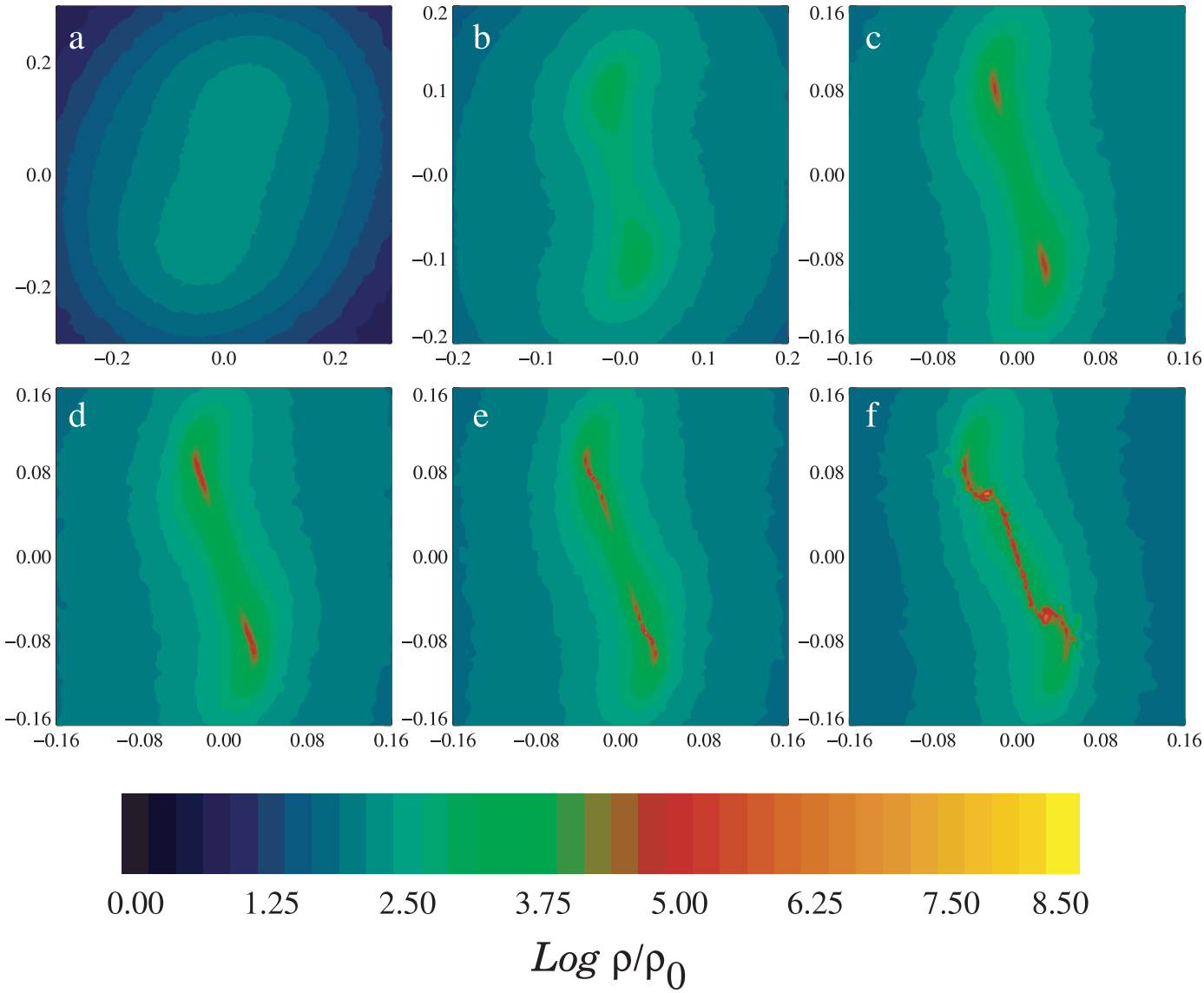

FIG. 2.—Column density images of the cloud midplane during the evolution of model U2A with 1.2 million particles. The times and peak densities are (*a*) $1.1146t_{\rm ff}$, 9.80×10^{-16} g cm^{-3}; (*b*) $1.2460t_{\rm ff}$, 9.37×10^{-15} g cm^{-3}; (*c*) $1.2658t_{\rm ff}$, 4.19×10^{-13} g cm^{-3}; (*d*) $1.2694t_{\rm ff}$, 6.93×10^{-12} g cm^{-3}; (*e*) $1.2748t_{\rm ff}$, 6.74×10^{-10} g cm^{-3}; and (*f*) $1.2910t_{\rm ff}$, 5.96×10^{-9} g cm^{-3}. The color denotes the density on a logarithmic scale. The axes are in units of the initial cloud radius.

higher than those required by the Jeans condition. We start by describing the results of models U1A and U2A, both with $\rho_{\rm crit} = 5.0 \times 10^{-12}$ g cm^{-3}. These two models differ only in their total number of SPH particles (see Table 1). Kitsionas & Whitworth (2002) showed that using 600,000 SPH particles, the collapse of the uniform cloud can be followed with an isothermal equation of state up to densities of $\sim 10^{-10}$ g cm^{-3}, without violating the Jeans condition. Recent resolution studies of the standard isothermal collapse test up to peak densities of 10^{-12} g cm^{-3}, using the newly written code GADGET-2 with 0.0355, 0.2681, 2.144, and 17.16 million particles, show that reasonably good convergence is seen for the calculations with 2.144 and 17.16 million particles, except for small residual differences in the evolution of the maximum density at earlier collapse times (Springel 2005). We note that 0.2681 million particles is less than half the number of particles employed by Kitsionas & Whitworth (2002), starting from which converged SPH solutions would be expected for the standard isothermal test case.

Figure 2 displays column density images of the cloud midplane during the collapse of model U2A through $\approx$9.2 orders of magnitude of increase in density. The evolution time is given in terms of the initial free-fall time ($\approx 1.07 \times 10^{12}$ s), and the calibration of the color scale is the same for all frames. For comparison, Truelove et al. (1998) performed highly resolved AMR calculations of this test model over a density increase of 8.1 decades, while Kitsionas & Whitworth (2002), using SPH methods, followed the same collapse over 8.9 decades in density. This model was also calculated by Boss et al. (2000), although with fixed finest resolution and to much lower central density contrasts (only 5 decades). The morphology of collapse for model U1A is almost undistinguishable from that depicted in Figure 2. Thus, a qualitatively converged solution is obtained when doubling the number of particles required to satisfy the Jeans condition, with the main difference being that model U2A progresses slightly faster than does model U1A because of its finer resolution.

The details of the initial phase of collapse are similar to those described by Bate & Burkert (1997). That is, collapse proceeds primarily down the rotation axis, while material in and near the central midplane undergoes a weak expansion perpendicular to the rotation axis, causing the formation of two overdense blobs

from the initial $m = 2$ perturbation seed. Soon after the end of the first free-fall time (by $\sim 1.044 t_{\rm ff}$), the expansion stops and the midplane region begins to collapse. As a result, the blobs fall toward the center and merge to form a prolate structure (Fig. 2*a* at $1.1146 t_{\rm ff}$). By this time, the overall cloud has already compressed into a flat disk with the inner bar being slightly denser at the endpoints. So, as the ends of the bar grow in mass, due to a converging gas flow onto them, they become self-gravitating and collapse upon themselves (Fig. 2*b*) to form a protostellar binary system, connected by a thin bar of lower density, as shown in Figure 2*c* at $1.2658 t_{\rm ff}$. At this epoch, the peak density ($\approx 4.19 \times 10^{-13}$ g cm^{-3}) is close to the values quoted by Truelove et al. (1998) in their Figure 12 ($\rho_{\rm max} \approx 3.91 \times 10^{-13}$ g cm^{-3} at $1.3167 t_{\rm ff}$) and Boss et al. (2000) in their Figure 6 ($\rho_{\rm max} \approx 4.0 \times 10^{-13}$ g cm^{-3} at $1.300 t_{\rm ff}$). In particular, we may see the strong resemblance of Figure 2*c* with Figure 12 of Truelove et al. (1998). The basic features of the formation of the binary and connecting bar are very similar between the two cases. Elongation of the fragments is already evident at these densities. Although no symmetries are imposed in our calculations, it is quite remarkable that to a good approximation, one fragment is the reflection of the other about the origin. Also, at the epoch of Figure 2*c*, the instantaneous separation between the fiducial centers of the fragments is $\approx 9.04 \times 10^{15}$ cm for model U1A and $\approx 9.06 \times 10^{15}$ cm for model U2A. For comparison, Truelove et al. (1998) quoted a separation of 9.2×10^{15} cm and Boss et al. (2000) found a distance of 1.1×10^{16} cm at comparable maximum densities. The subsequent isothermal collapse of the elongated fragments proceeds in an approximate cylindrical manner toward formation of a linear singularity (Inutsuka & Miyama 1992). Figures 2*d* (at $1.2694 t_{\rm ff}$) and 2*e* (at $1.2748 t_{\rm ff}$) show the cloud center when the maximum density has passed $\rho_{\rm crit}$. The binary components and the bar connecting them approximate to filamentary singularities. Figure 2*d* shows good qualitative agreement with the results of Kitsionas & Whitworth (2002) in their Figure 1*a* at comparable peak densities. Also, note that the long filamentary shape of the fragments, visible in Figure 2*e*, strongly resembles that depicted by Truelove et al. (1998) in their Figure 13 by the time the density has raised over ~ 8 decades in both cases. During this stage, the gas within the fragments has become adiabatic and is heating up. The breakdown of isothermality slows down the cylindrical collapse of the fragments and forces them to a reduction of dimensionality from an almost one-dimensional linear object to a quasi-spherical, essentially pointlike one. This feature is evident in Figure 2*f* ($1.2910 t_{\rm ff}$), when the peak density has increased over 9.2 decades.

Figure 3 depicts the position of particles in the cloud midplane toward the end of the calculation for models U1A (Fig. 3*a*) and U2A (Fig. 3*b*) at comparable maximum densities. Evident in these figures is the fanning-out of the bar close to the quasi-spherical binary fragments. Similar features were also observed by Kitsionas & Whitworth (2002). They argued that this effect is a real one due to tidal shearing of the bar by the inspiraling binary fragments. In both cases, however, the bar is still isothermal and continues to evolve to a singular filament with no signs of fragmentation. A more quantitative comparison between models U1A and U2A is given in Figure 4, where the mass of the binary fragments and their ratios of the thermal (α) and rotational (β) energy over the absolute value of the gravitational energy are plotted as functions of time. With this purpose, the fragment volume is approximately defined by the region around the particle of maximum density that is occupied by all surrounding particles with densities higher than a factor f of the maximum density, where f was assumed to vary monotonically with time between 0.5 (at the epoch of fragment formation) and 0.1 (by the time the fragment starts collapsing upon itself and evolving as a separate entity). This criterion for choosing f has been employed in most previous work and therefore we adopt it here. The mean mass of a fragment is then obtained by summing over the masses of all particles lying within this volume. Estimates of the thermal, rotational, and gravitational energies associated with the fragment volume are then obtained by means of the summations

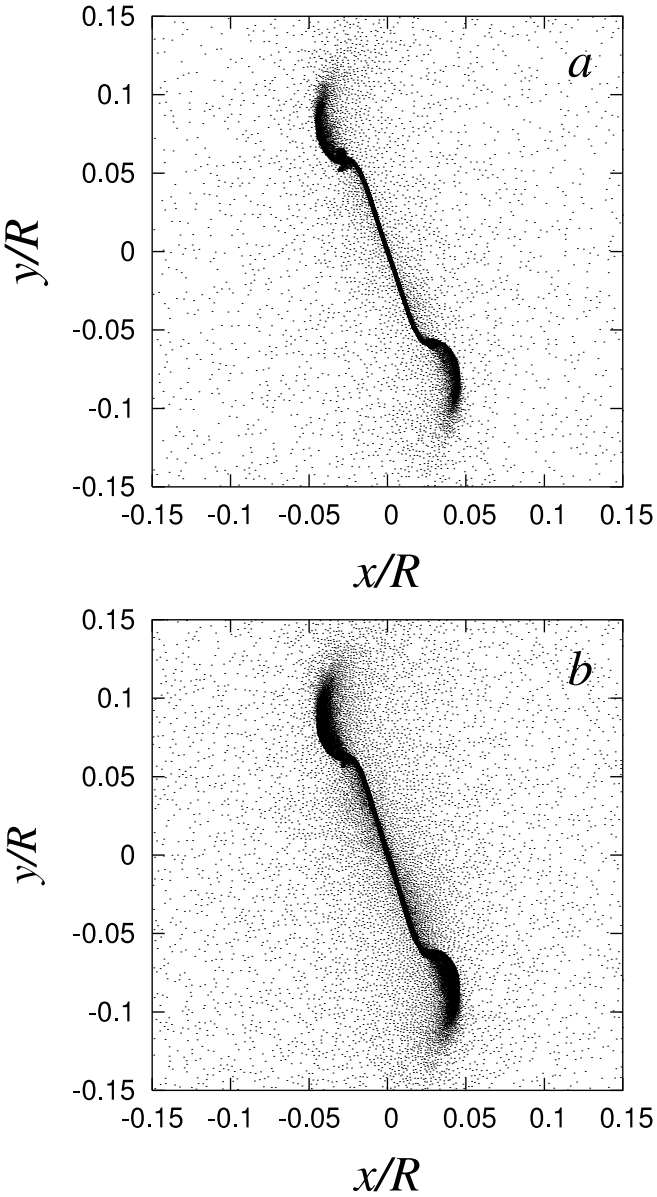

Fig. 3.—Positions of particles lying within a slice of thickness $\Delta z/R = 5 \times 10^{-4}$ about the cloud midplane ($z = 0$). The binary core and the thin filament connecting them are shown for (*a*) model U1A at $1.291 t_{\rm ff}$ when $\rho_{\rm max} \approx 3.76 \times 10^{-9}$ g cm^{-3} and (*b*) model U2A at $1.286 t_{\rm ff}$ when $\rho_{\rm max} \approx 3.60 \times 10^{-9}$ g cm^{-3}. A total number of 58,982 and 113,820 particles are shown in (*a*) and (*b*), respectively.

$$E_{\rm ther} = \frac{3}{2} \sum_i m_i \frac{p_i}{\rho_i},$$
$$E_{\rm rot} = \frac{1}{2} \sum_i m_i v_{\phi_i}^2, \qquad (14)$$
$$E_{\rm grav} = \frac{1}{2} \sum_i m_i \Phi_i,$$

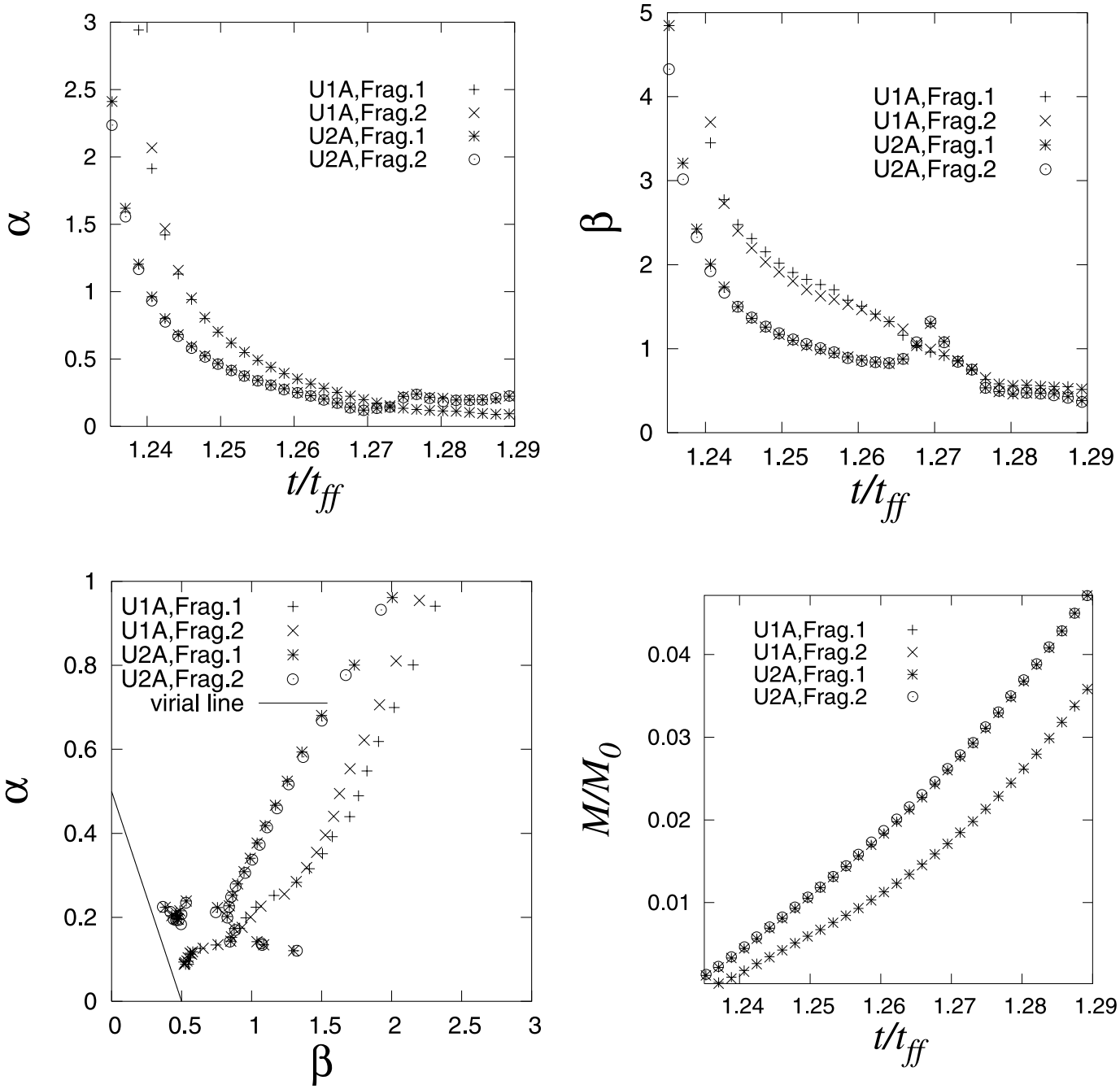

FIG. 4.—Time evolution of the thermal (α; *top left*) and rotational energy (β; *top right*) to the absolute value of the gravitational energy for the binary fragments of models U1A and U2A. The bottom panels show their tracks in the (α, β)-plane (*bottom left*) and their growing masses in units of the initial cloud mass (*bottom right*). The plus signs and crosses apply to model U1A, while the asterisks and dotted circles apply to model U2A. The solid line in the bottom left panel marks the line of virial equilibrium ($\alpha + \beta = 0.5$).

respectively, where Φ_i is the value of the gravitational potential at the location of particle i, v_{ϕ_i} refers to the ϕ-velocity component for that particle with respect to a fixed axis passing through the particle of maximum density, and the summations include the contributions from all particles pertaining to the fragment volume. It is clear from Figure 4 that the binary components in each model are essentially identical and share almost the same evolution. After the onset of fragmentation, the binary clumps of model U2A have lower values of α (*top left panel*) and β (*top right panel*), compared to model U1A at similar evolutionary times. This is one effect of fragmentation occurring slightly earlier in model U2A because of its finer resolution. However, after about $1.27t_{\rm ff}$, when the fragments are already collapsing upon themselves, the evolution of α and β for both runs exhibits a closer convergence. The bottom left panel shows the evolution of the fragments in the (α, β)-plane, where they are seen to approach a state of virial equilibrium by the end of the calculations. Moreover, the filament plus binary system for model U1A is less massive ($\approx 0.112\ M_\odot$) than for model U2A ($\approx 0.143\ M_\odot$), while the fragments contain $\sim$7.4% of the total cloud mass in model U1A and $\sim$8.5% in model U2A, as we may see from Table 2, where the fragment properties at the end of the calculations are listed for the uniform models. Finally, the solid (case U1A) and dashed (case U2A) lines in Figure 8 show the

TABLE 2
FRAGMENT PROPERTIES FOR THE UNIFORM CLOUDS

Model	Time (t_{ff})	M_f/M_0	$M_{tot,f}/M_0$	α	β
U1A.....	1.2910	0.0372	0.0745	0.107	0.468
		0.0373	...	0.104	0.470
U2A.....	1.2860	0.0426	0.0853	0.157	0.412
		0.0427	...	0.155	0.414
U1B.....	1.3999	0.0935	0.1896	0.195	0.321
		0.0961	...	0.193	0.327
U2B.....	1.3955	0.0929	0.1832	0.244	0.287
		0.0903	...	0.249	0.272

maximum density as a function of time. Reasonably good convergence is achieved between these two curves. Only very small residual differences are visible in the evolution just after the first free-fall time, which is consistent with the fact that model U2A evolves to higher densities slightly faster than does model U1A.

Models U1B and U2B differ from the previous cases in that $\rho_{crit} = 5.0 \times 10^{-14}$ g cm^{-3}, so that the isothermal phase of collapse is assumed to be shorter. Up to the time when $\rho_{max} \approx \rho_{crit}$, the evolution is the same as described before. SPH calculations of this model at much lower resolution were performed by Bate & Burkert (1997). Later on, Klein et al. (1999) recalculated the same collapse using their adaptive AMR code. Figures 5 and 6 show column density images of the cloud midplane during the collapse of models U1B and U2B, respectively, starting from the point where isothermality breaks down. Binary fragmentation is already evident when ρ_{max} exceeds ρ_{crit} (Figs. 5*a* and 6*a*). However, unlike models U1A and U2A, adiabatic collapse impedes the fragment region to approximate a filamentary singularity (Figs. 5*b* and 6*b*). A prominent bar has also formed between the fragments, which soon becomes optically thick. As a result, the overwhelming pressure forces slow down and then stop further collapse of the bar upon itself (Figs. 5*c* at $1.3144t_{ff}$ and 6*c* at $1.3212t_{ff}$). At this stage, the binary core and the bar are both embedded in a long two-armed spiral, reminiscent of the initial $m = 2$ perturbation. In the subsequent evolution, the binary

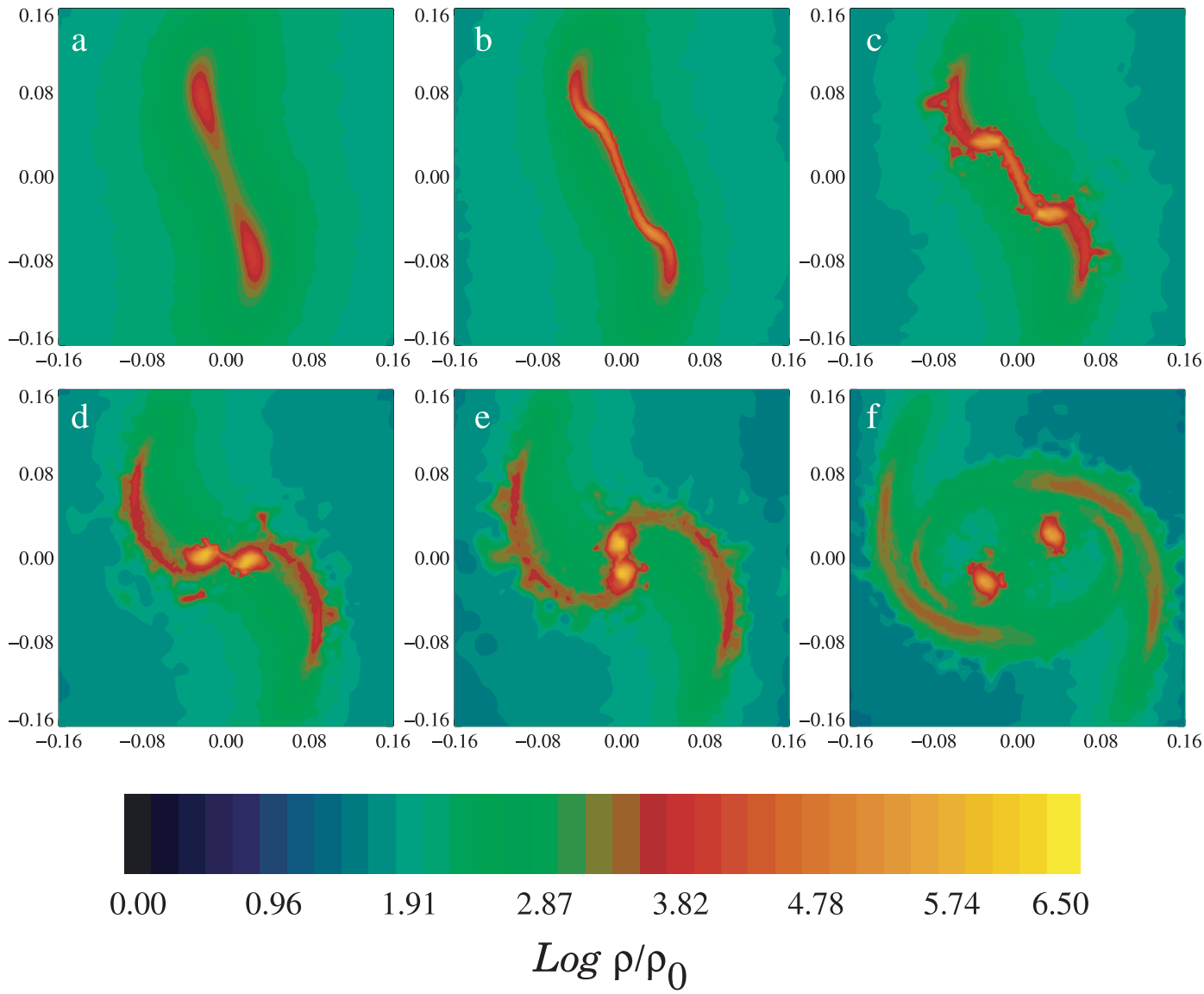

FIG. 5.—Column density images of the cloud midplane during the evolution of model U1B with 600,000 particles. The times and peak densities are (*a*) $1.2739t_{ff}$, 5.42×10^{-14} g cm^{-3}; (*b*) $1.2964t_{ff}$, 7.86×10^{-13} g cm^{-3}; (*c*) $1.3144t_{ff}$, 3.65×10^{-12} g cm^{-3}; (*d*) $1.3414t_{ff}$, 5.17×10^{-12} g cm^{-3}; (*e*) $1.3594t_{ff}$, 7.08×10^{-12} g cm^{-3}; and (*f*) $1.3999t_{ff}$, 8.79×10^{-12} g cm^{-3}. The color denotes the density on a logarithmic scale. The axes are in units of the initial cloud radius.

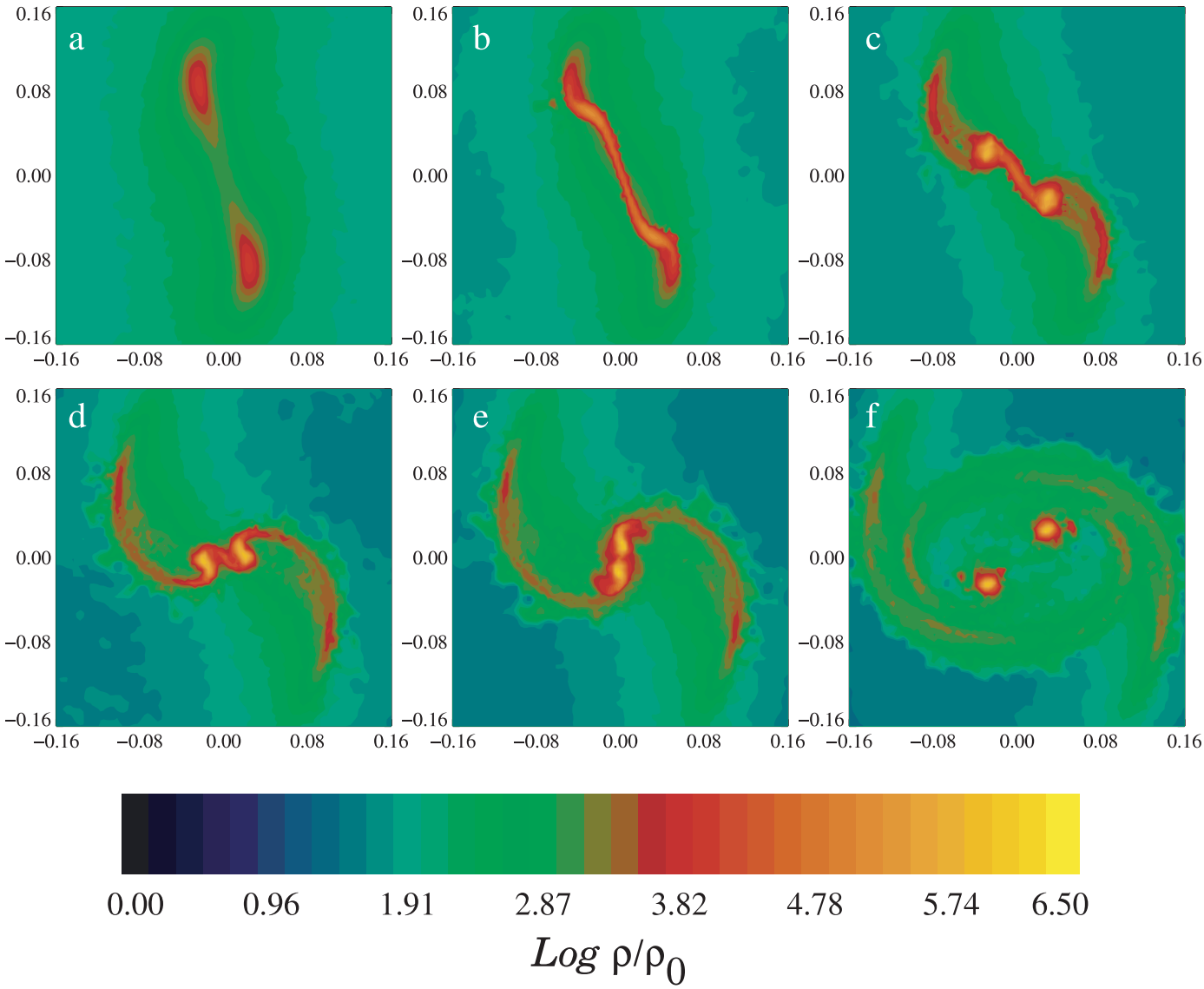

FIG. 6.—As in Fig. 5, but for model U2B with 1.2 million particles. The times and peak densities are (*a*) $1.2626t_{\rm ff}$, 5.31×10^{-14} g cm^{-3}; (*b*) $1.2897t_{\rm ff}$, 7.36×10^{-13} g cm^{-3}; (*c*) $1.3212t_{\rm ff}$, 3.50×10^{-12} g cm^{-3}; (*d*) $1.3437t_{\rm ff}$, 5.11×10^{-12} g cm^{-3}; (*e*) $1.3549t_{\rm ff}$, 7.44×10^{-12} g cm^{-3}; and (*f*) $1.3955t_{\rm ff}$, 1.36×10^{-11} g cm^{-3}. The color denotes the density on a logarithmic scale. The axes are in units of the initial cloud radius.

fragments are pulled inward due to accretion of low angular momentum gas from the bar. After a quarter-orbit of the fragments, the trailing spiral arms warp up and elongate by the time the bar has almost dissipated and the binary has come close together (Figs. 5*d* at $1.3414t_{\rm ff}$ and 6*d* at $1.3437t_{\rm ff}$). Later on, when $\rho_{\rm max} \approx 7.08 \times 10^{-12}$ g cm^{-3} (case U1B) and $\approx 7.44 \times 10^{-12}$ g cm^{-3} (case U2B), the binary core reaches its closest orbital separation (Figs. 5*e* at $1.3594t_{\rm ff}$ and 6*e* at $1.3549t_{\rm ff}$), which is ~90 AU for model U1B and ~89 AU for model U2B. Note that each binary component is accompanied by protostellar disks, which accrete primarily high angular momentum mass directly from the long spiral arms. The fragments in turn accrete mass from the disks and start separating from each other, while the trailing spiral arms wind up and form a dense circumbinary disk (Figs. 5*f* at $1.3999t_{\rm ff}$ and 6*f* at $1.3955t_{\rm ff}$). At this stage, the cores are fully detached with an instantaneous separation of ~302 AU for model U1B and ~262 AU for model U2B. The protostellar disks remain attached to the long spiral and have average radii of ~100 AU, while the circumbinary disk extends over a mean diameter of ≈660 AU for model U1B and ≈680 AU for model U2B. The morphology of collapse and fragmentation is very similar to that obtained by Klein et al. (1999) with their AMR code. In particular, the final binary protostellar disk/core system in Figures 5*f* and 6*f* bears a strong resemblance with their Figure 6 at $1.4816t_{\rm ff}$. At the moment of closest binary approach they quote a separation of ~44 AU (their Fig. 3), which is a factor of $\frac{1}{2}$ smaller than those found for models U1B and U2B. Also, the peak density in their Figure 6 is about an order of magnitude higher than in Figures 5*f* and 6*f*, while the final binary separation is ~400 AU compared to ~302 AU for Figure 5*f* and ~262 AU for Figure 6*f*.

The cores contain ~19% (model U1B) and ~18% (model U2B) of the mass of the initial cloud (see Table 2). Figure 7 depicts the time evolution of the fragment properties and their tracks in the (α, β)-plane. It is clear from these figures that for both models the fragments follow similar evolutions and that they approach a state of virial equilibrium by the end of the calculations. For comparison, Klein et al. (1999) report that about 20% of the total cloud mass is in the form of binary fragments at the time of their Figure 6. Moreover, Figure 8 shows that reasonably good convergence is achieved for models U1B (*dotted line*) and U2B (*dot-dashed line*),

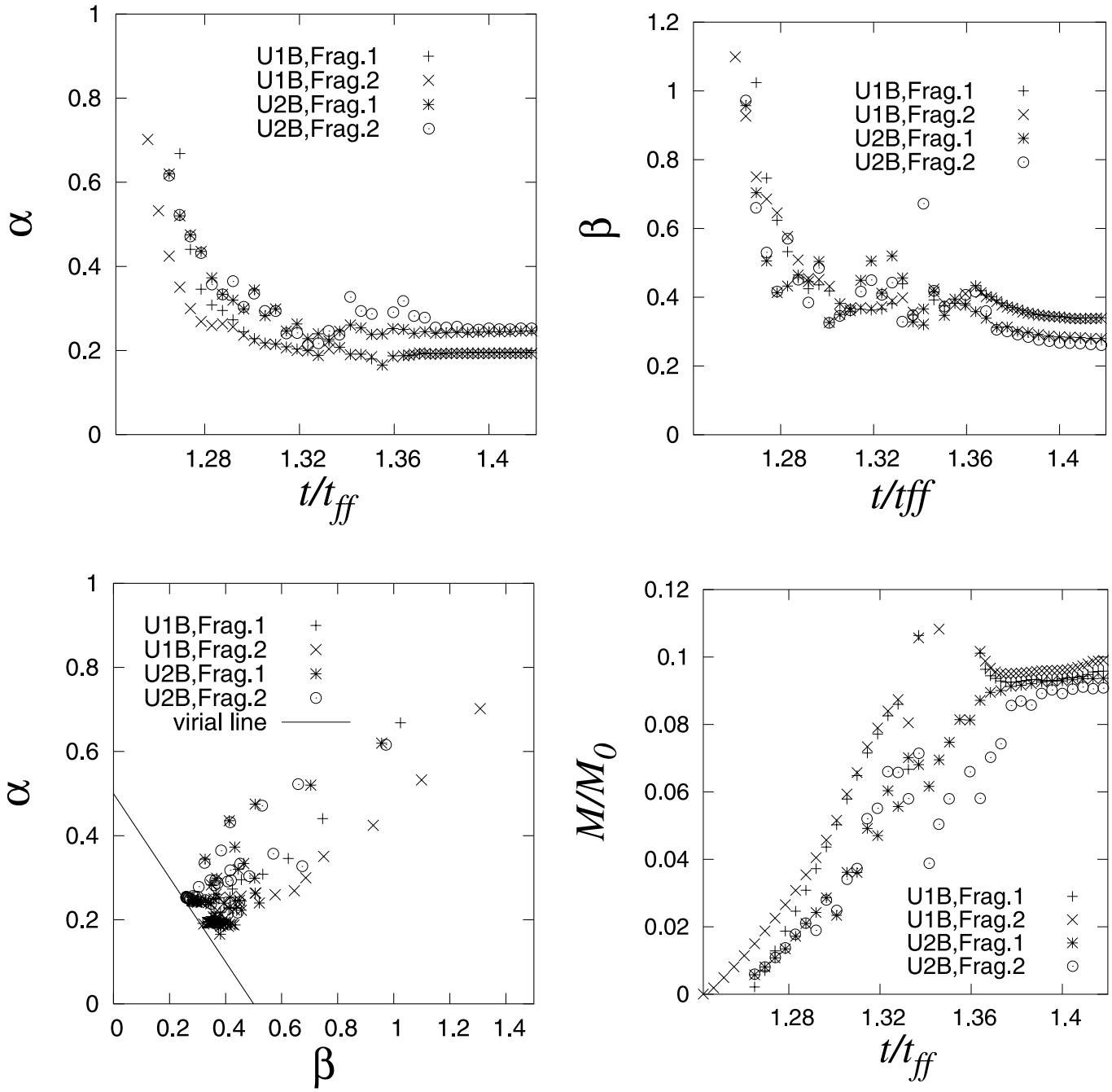

FIG. 7.—Integral properties of the binary fragments for models U1B and U2B as functions of time. In each panel, the plus signs and crosses apply to model U1B, while the asterisks and dotted circles apply to model U2B. The solid line in the bottom left panel marks the line of virial equilibrium ($\alpha + \beta = 0.5$).

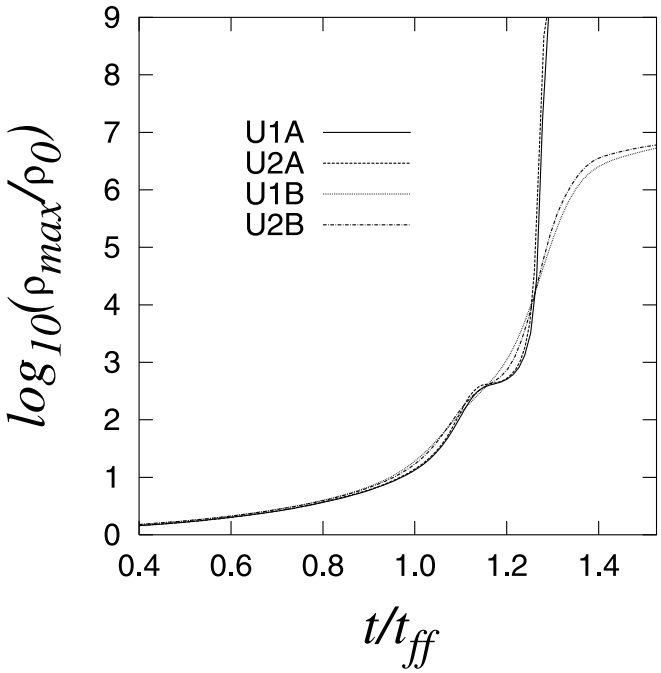

FIG. 8.—Time evolution of the maximum density for models U1A (*solid line*), U2A (*dashed line*), U1B (*dotted line*), and U2B (*dot-dashed line*).

with only small differences toward the later phases of collapse when the maximum densities for model U2B are slightly higher than for model U1B. As for models U1A and U2A, in this case convergence is also seen when doubling the number of particles required to satisfy the Jeans condition. Independently of whether the transition from isothermal to adiabatic collapse is anticipated or retarded, the uniform cloud leads to a binary system, implying that thermal retardation plays no role in either enhancing fragmentation or changing the number of fragments. However, thermal retardation results in more massive fragments due to enhanced mass accretion.

4.2. *Collapse of Gaussian Clouds*

We now turn to the collapse of the Gaussian cloud first calculated by Boss (1991). This model was recalculated at high spatial resolution with the aid of adaptive FD codes by Burkert & Bodenheimer (1996), Truelove et al. (1997), Boss (1998), and Sigalotti & Klapp (2001b, 2001c), using an isothermal equation of state, and by Boss et al. (2000), who performed two independent calculations: one with a barotropic equation of state and the other by including nonisothermal thermodynamics, with Eddington-approximation radiative transfer and detailed equations of state, to model the transition from isothermal to nonisothermal collapse. While a fairly good agreement has been established that the outcome of the isothermal collapse is a singular filament, as yet no definite solution has been reached when nonisothermal (adiabatic) effects are included. In particular, the calculations of Boss et al. (2000) showed that in the barotropic approximation (their model B&M-B) the cloud collapsed to form a thin filament, which shortly thereafter fragmented into two weak clumps by the time $\rho_{\max} = 1.3 \times 10^{-11}$ g cm^{-3}. However, the subsequent evolution could not be followed because of limitations with their spherical-coordinate code to solve fine-scale structure. When the same model was rerun with their adaptive AMR code, a nearly identical thin filament formed, containing two weakly defined clumps, at about the same maximum density as the B&M-B model. When the AMR calculation was evolved further in time toward a peak density of 1.0×10^{-9} g cm^{-3}, the two clumps converged to the center and merged into a single, central core surrounded by trailing spiral arms. In contrast, the radiative-transfer collapse calculation (their model B&M-E) produced a central clump surrounded by spiral arms containing two more clumps at a maximum density of 5.0×10^{-11} g cm^{-3}. The actual fate of the triple system could not be assessed because they were unable to continue the collapse farther in time with their radiative transfer code. In passing, we note that so far no SPH calculations of the Gaussian cloud have been reported in the literature.

In this section we describe the results obtained for the barotropic collapse of the Gaussian cloud for two distinct sequences of model calculations, the details of which are listed in Table 1. The aim of the present models is to explore (1) the convergence of the intermediate phases of collapse with the FD simulations of Boss et al. (2000), (2) the level of resolution needed with SPH to achieve convergence, and (3) the sensitivity of fragmentation to the effects of thermal retardation due to nonisothermal heating. We start the discussion with models G1A–G6A, which refer to six identical simulations with $\rho_{\rm crit} = 5.0 \times 10^{-12}$ g cm^{-3} and a differing number of particles (see Table 1). For comparison, the calculations of Boss et al. (2000) used $\rho_{\rm crit} = 3.16 \times 10^{-12}$ g cm^{-3}. Figure 9 shows column density images of the cloud midplane for the evolution of model G6A with 10 million particles. An almost identical evolution was also followed by model G5A, using 5 million particles. The cloud collapses isothermally to form a central prolate core (Figs. 9*a* and 9*b*). Soon thereafter, the innermost core enters a phase of adiabatic collapse, while the surrounding regions remain approximately isothermal and continue to experience cylindrical collapse. During this phase, the AMR calculations of Boss et al. (2000) lead to the formation of a thin filament, containing two weak density maxima (their Fig. 5*c* at $\rho_{\max} = 2.5 \times 10^{-11}$ g cm^{-3}). A quite similar filament is also obtained with GADGET-2, as shown in Figure 9*c* at the same peak density. In the present case, however, no embedded binary clumps are evident. As the central gas heats up, the filament stops its cylindrical collapse and becomes distorted because of differential rotation. Meanwhile a central adiabatic core forms (Fig. 9*d*). By the time the maximum density has grown to 5.5×10^{-10} g cm^{-3} (Fig. 9*e*), trailing spiral arms have developed around the central core. This structure is also very similar to that shown by Boss et al. (2000) in their Figure 5*d* when $\rho_{\max} = 1.0 \times 10^{-9}$ g cm^{-3}. However, when the GADGET-2 calculation is evolved to such peak density, the orbiting spiral arms surrounding the central core quickly deform and expand away because of rotational effects (Fig. 9*f*). At this time, a number of small clumps appear to be condensing from the distorted spirals. Continuation of the calculation up to $\rho_{\max} = 2.54 \times 10^{-9}$ g cm^{-3} shows the formation of a final central core embedded in a dense two-armed spiral. Figure 10 displays images of the final configurations obtained for models G1A–G6A at such maximum density, when the calculations are terminated. Models G1A (Fig. 10*a*) to G3A (Fig. 10*c*) clearly lead to small-scale structures that differ in shape from one another. According to the analysis of Attwood et al. (2007), the lack of convergence suggests that for these models the ratio $N_{\rm tot}/N_{\rm neigh}$ was not sufficiently large to avoid numerical dissipation and for diffusion to take place over the evolution timescale. As the total number of particles is increased from 3 million (case G4A; Fig. 10*d*) to 10 million (case G6A; Fig. 10*f*), convergence is achieved on qualitative grounds because the timescales of numerical dissipation and diffusion become at least comparable to the evolution time. In particular, Figures 10*e* (model G5A) and 10*f* (model G6A) look almost identical, meaning that true convergence is obtained for this Gaussian-cloud collapse when working with 5–10 million particles. The two-armed spiral has a

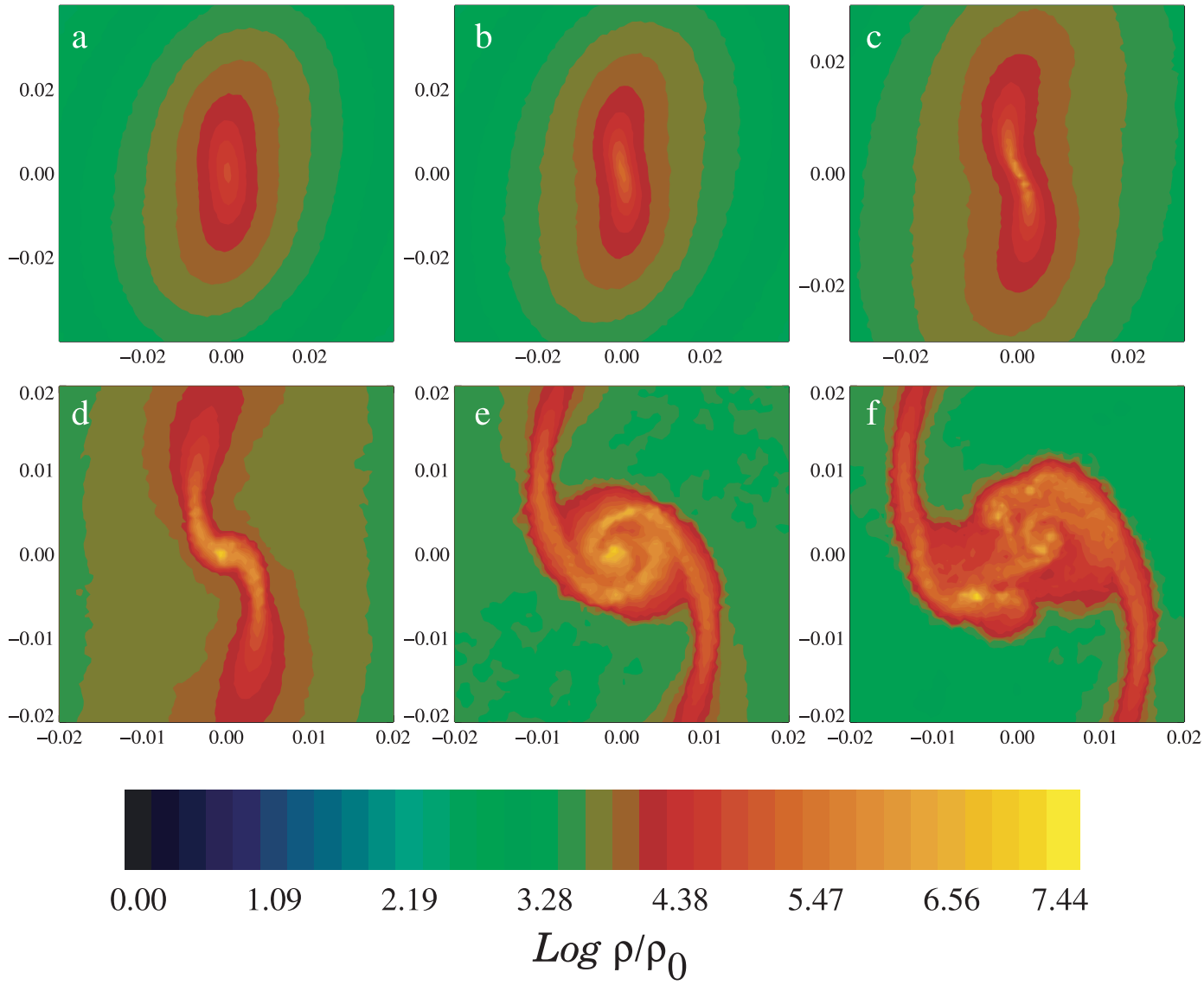

FIG. 9.—Column density images of the cloud midplane during the evolution of model G6A with 10 million particles. The times and peak densities are (*a*) $1.3675t_{\rm ff}$, 2.84×10^{-13} g cm^{-3}; (*b*) $1.3728t_{\rm ff}$, 1.05×10^{-12} g cm^{-3}; (*c*) $1.3782t_{\rm ff}$, 2.55×10^{-11} g cm^{-3}; (*d*) $1.3865t_{\rm ff}$, 1.71×10^{-10} g cm^{-3}; (*e*) $1.4150t_{\rm ff}$, 5.51×10^{-10} g cm^{-3}; and (*f*) $1.4368t_{\rm ff}$, 1.02×10^{-9} g cm^{-3}. The color denotes the density on a logarithmic scale. The axes are in units of the initial cloud radius.

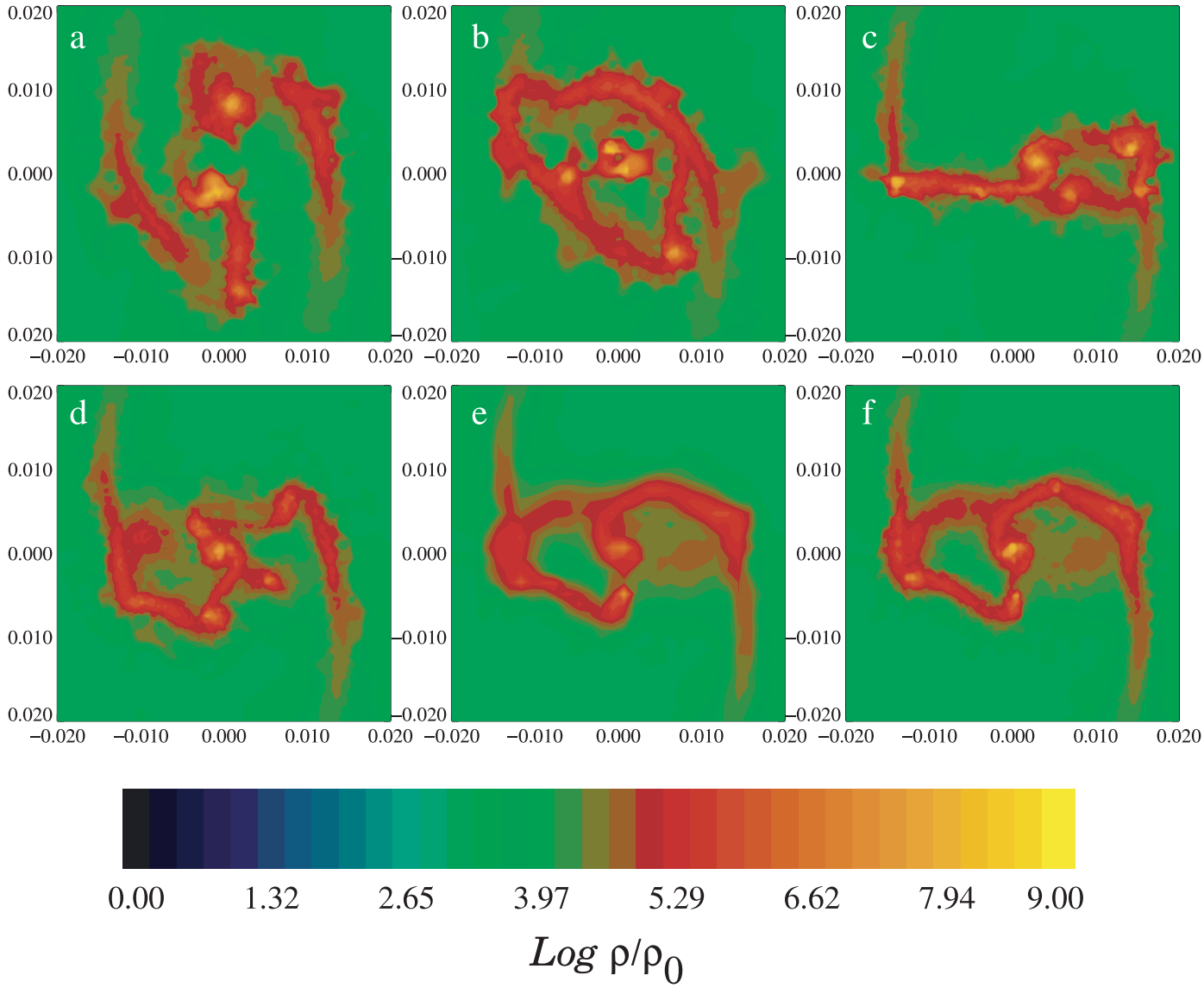

FIG. 10.—Column density images of the cloud midplane showing the final configuration obtained for models (*a*) G1A ($1.4879t_{\rm ff}$), (*b*) G2A ($1.4723t_{\rm ff}$), (*c*) G3A ($1.4697t_{\rm ff}$), (*d*) G4A ($1.4434t_{\rm ff}$), (*e*) G5A ($1.4423t_{\rm ff}$), and (*f*) G6A ($1.4418t_{\rm ff}$). In all frames, the maximum density is 2.54×10^{-9} g cm^{-3}. The color denotes the density on a logarithmic scale. The axes are in units of the initial cloud radius.

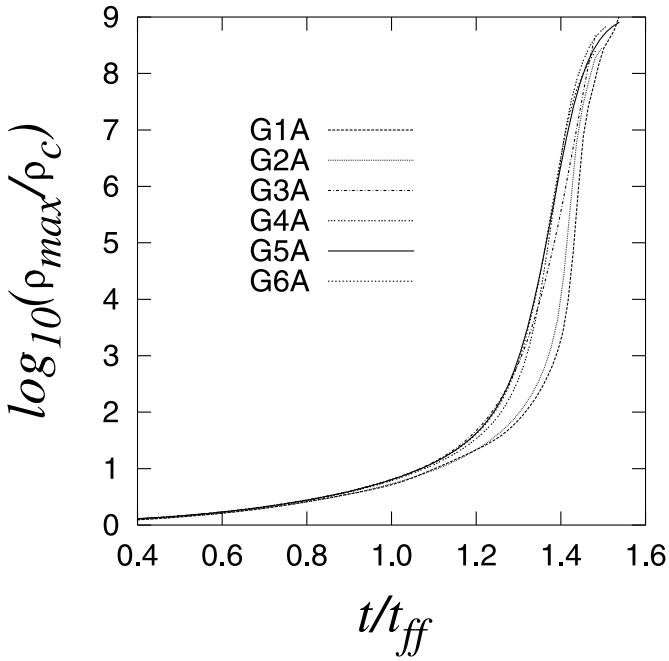

FIG. 11.—Time evolution of the maximum density for models G1A–G6A. The legend within the box specifies the model to which each curve corresponds.

TABLE 3

FRAGMENT PROPERTIES FOR THE GAUSSIAN CLOUDS

Model	Time (t_{ff})	M_f/M_0	$M_{tot,f}/M_0$	α	β
G1A	1.4879	0.0079	0.0114	0.136	0.462
		0.0035	...	0.172	0.437
G2A	1.4723	0.0039	0.0084	0.202	0.320
		0.0026	...	0.239	0.350
		0.0019	...	0.235	0.380
G3A	1.4697	0.0056	0.0126	0.153	0.351
		0.0038	...	0.194	0.406
		0.0031	...	0.205	0.415
G4A	1.4434	0.0061	0.0110	0.251	0.447
		0.0046	...	0.156	0.343
G5A	1.4423	0.0063	0.0063	0.156	0.356
G6A	1.4418	0.0061	0.0061	0.152	0.384
G1B	1.8011	0.0401	0.0797	0.229	0.261
		0.0207	...	0.435	0.224
		0.0190	...	0.476	0.190
G2B	1.8252	0.0396	0.0833	0.245	0.263
		0.0233	...	0.422	0.238
		0.0204	...	0.413	0.184
G3B	1.8613	0.0371	0.1023	0.280	0.251
		0.0224	...	0.397	0.257
		0.0215	...	0.385	0.321
		0.0213	...	0.348	0.318
G4B	1.8091	0.0510	0.0966	0.252	0.373
		0.0456	...	0.314	0.294
G5B	1.8110	0.0494	0.0969	0.269	0.314
		0.0475	...	0.279	0.318
G6B	1.8072	0.0480	0.0938	0.243	0.288
		0.0458	...	0.266	0.259

well-defined clumpy structure, suggesting that further fragmentation may eventually occur. However, by the times of Figures 10*e* and 10*f* the small clumps have masses lower than $\sim 5.0 \times 10^{-4}$ times the initial cloud mass and so they cannot be considered true fragments. The time evolutions of the maximum density for models G1A–G6A are compared in Figure 11. That models G5A and G6A essentially converge to the same solution can be seen by the solid line (model G5A) overlapping the short-dashed curve (model G6A), except toward the end of the calculation when model G6A attains slightly higher densities compared to model G5A because of its finer resolution. Table 3 lists the fragment properties for the Gaussian clouds at the termination of the calculations. Note that only $\sim$0.6% of the total cloud mass is contained by the central adiabatic core.

We now describe the results for models G1B–G6B, which differ from the previous sequence in that the isothermal phase of collapse is assumed to be shorter (i.e., $\rho_{crit} = 5.0 \times 10^{-14}$ g cm^{-3}). The time history of model G6B with 10 million particles is depicted in Figure 12. Models G4B and G5B with a lower number of particles evolved in quite similar fashion. Up to the point where $\rho_{max} = \rho_{crit}$, the cloud evolves into a centrally condensed, flat disk as before. As the central cloud regions enter the adiabatic phase of collapse, a differentially rotating bar develops (Fig. 12*a*), whose maximum density is about 2 orders of magnitude lower than in model G6A (Fig. 9*c*) because of thermal retardation. The bar inflates due to the deforming effects of rotation and the increased pressure gradients that slow down the collapse. As a result, the central bar warps up, develops two weak density maxima, and evolves to a transient elliptical disk with trailing spiral arms (Fig. 12*b*). Later on, because of further rotation the disk soon becomes S-shaped and the two density peaks fall toward the center (Fig. 12*c*). After rotating for more than 90°, the S-shaped structure grows in size and develops long arms connected by a central dense bar (Fig. 12*d*). The bar accretes mass directly from the arms and starts fragmenting into two clumps (Fig. 12*e*). At this time, the end parts of the winding arms evolve into two more ("satellite") condensations, which are confined by self-gravity. Fragmentation of the bar leads to a well-defined inner binary (Fig. 12*f*). In contrast, for models G1B and G2B, working with 0.6 and 1.2 million particles, respectively, the central bar decayed into a central blob without ever fragmenting. Meantime, the satellite fragments condense and take the form of an outer binary (Fig. 12*g*). The inner binary rotates at a faster rate and detaches, while the outer binary follows a nearly circular orbit and accretes mass from the outer disk, coming close together (Fig. 12*h*). As the inner binary further detaches, its components merge with those of the outer binary. As a result a wide binary system forms, as shown in Figure 12*i*, when $\rho_{max} = 1.39 \times 10^{-11}$ g cm^{-3}. Figure 13 compares the outcome of the evolution for models G1B–G6B at comparable maximum densities ($\gtrsim 1.4 \times 10^{-11}$ g cm^{-3}), when the calculations were terminated. Evidently, good convergence is reached for models G5B (Fig. 13*e*) and G6B (Fig. 13*f*), working with 5 and 10 million particles, respectively. The evolution of the maximum density for all six models is depicted in Figure 14, where only the curves for models G5B (*solid line*) and G6B (*short-dashed line*) exhibit a closer correspondence.

Models G1B and G2B formed a ternary system (Figs. 13*a* and 13*b*), while model G3B (Fig. 13*c*) formed a quadruple core. The difference in the number of final fragments is due to the fact that for the former models the central bar did not fragment but rather decayed into a single blob. It may well be that the quadruple system for model G3B could eventually decay into a binary core, as in models G4B–G6B, due to pairwise merging of the component fragments later in the evolution. The wide binaries in models G5B and G6B have mean separations of $\sim$300 AU and masses of $\sim 1.0\ M_\odot$ each, representing about 10% of the total initial cloud mass. The properties of these fragments at the times of

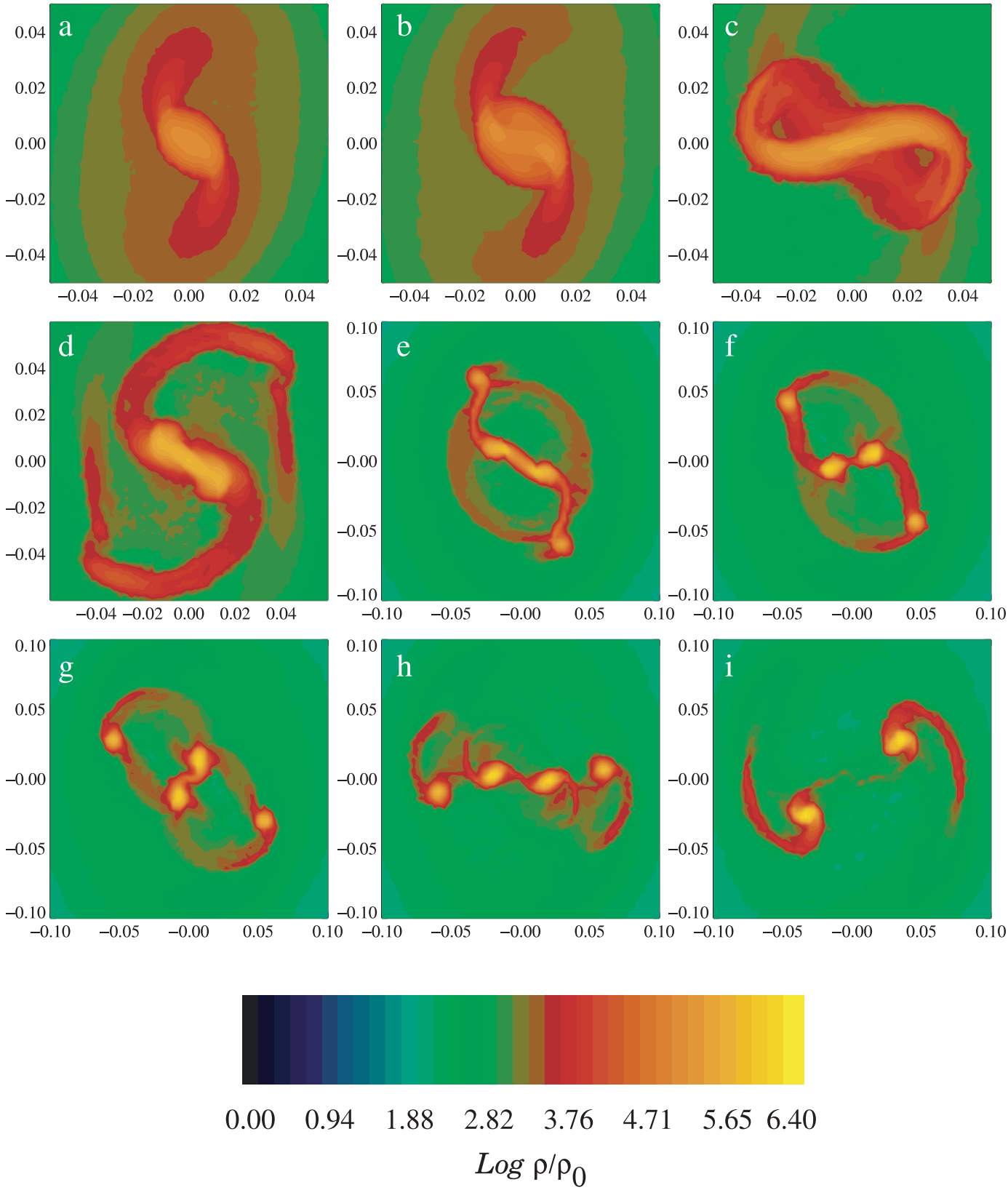

FIG. 12.—Column density images of the cloud midplane during the evolution of model G6B with 10 million particles. The times and peak densities are (*a*) $1.4244t_{\rm ff}$, 5.96×10^{-13} g cm^{-3}; (*b*) $1.4434t_{\rm ff}$, 6.51×10^{-13} g cm^{-3}; (*c*) $1.5574t_{\rm ff}$, 1.37×10^{-12} g cm^{-3}; (*d*) $1.6248t_{\rm ff}$, 2.93×10^{-12} g cm^{-3}; (*e*) $1.6913t_{\rm ff}$, 4.36×10^{-12} g cm^{-3}; (*f*) $1.7130t_{\rm ff}$, 7.61×10^{-12} g cm^{-3}; (*g*) $1.7283t_{\rm ff}$, 8.85×10^{-12} g cm^{-3}; (*h*) $1.7663t_{\rm ff}$, 1.17×10^{-11} g cm^{-3}; and (*i*) $1.8043t_{\rm ff}$, 1.39×10^{-11} g cm^{-3}. The color denotes the density on a logarithmic scale. The axes are in units of the initial cloud radius.

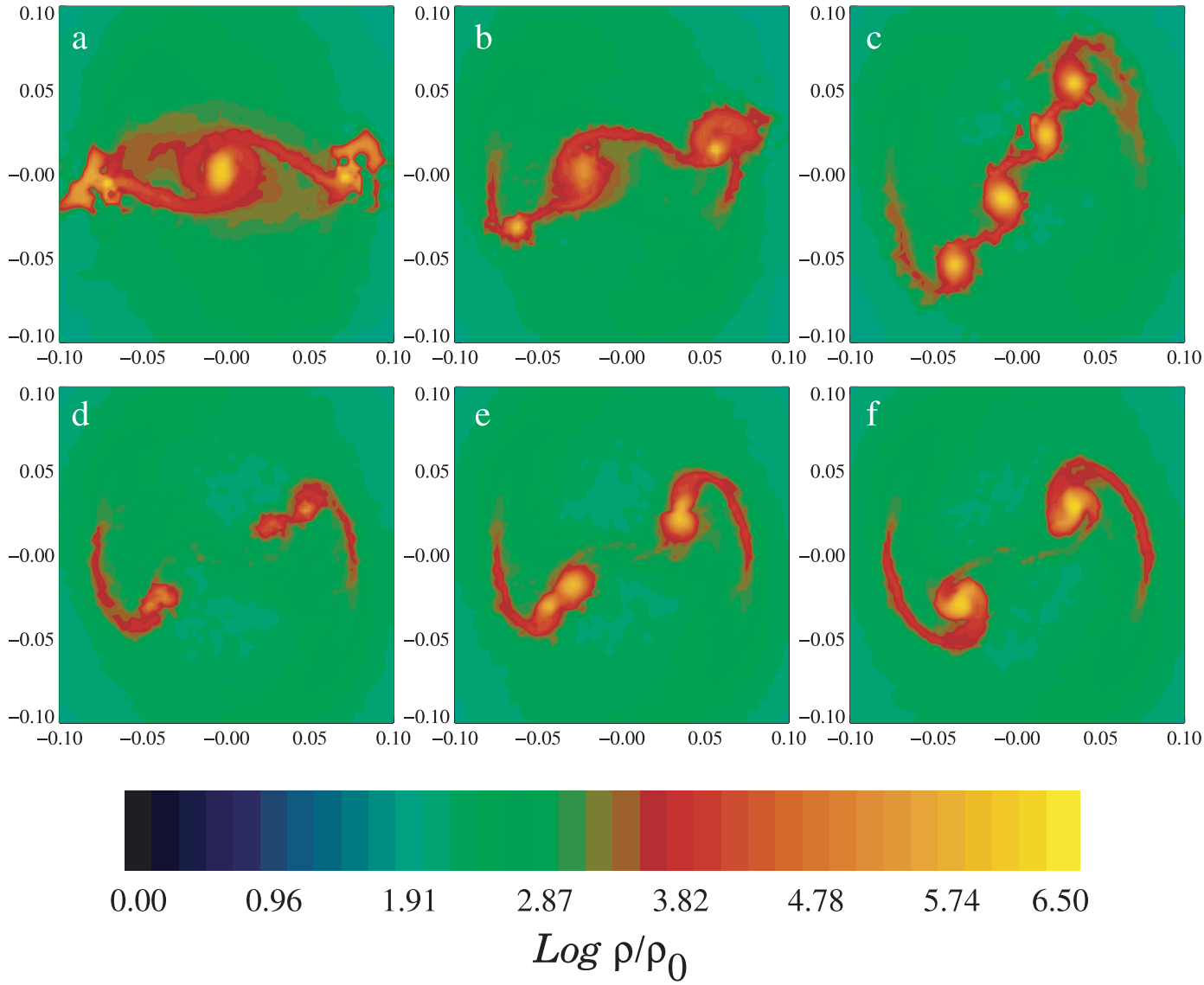

FIG. 13.—Column density images of the cloud midplane showing the final configuration obtained for models (*a*) G1B ($1.8011t_{\rm ff}$), (*b*) G2B ($1.8252t_{\rm ff}$), (*c*) G3B ($1.8613t_{\rm ff}$), (*d*) G4B ($1.8091t_{\rm ff}$), (*e*) G5B ($1.8110t_{\rm ff}$), and (*f*) G6B ($1.8072t_{\rm ff}$). The maximum densities are (*a*) 1.43×10^{-11} g cm^{-3}, (*b*) 1.45×10^{-11} g cm^{-3}, (*c*) 1.43×10^{-11} g cm^{-3}, (*d*) 1.42×10^{-11} g cm^{-3}, (*e*) 1.46×10^{-11} g cm^{-3}, and (*f*) 1.44×10^{-11} g cm^{-3}. The color denotes the density on a logarithmic scale. The axes are in units of the initial cloud radius.

Figure 13 are listed in Table 3. At least during the early phases of collapse, thermal retardation seems to favor fragmentation of the Gaussian cloud, leading to an increased number of fragments at least for those runs where convergence is attained. However, it is clear from the results of models G5A and G6A that further fragmentation may well occur late in the evolution so that thermal retardation may indeed not play a role in determining the final number of protostars.

5. CONCLUSIONS

In this paper, we have calculated the early phases of cloud collapse and fragmentation up to the formation of the first protostellar core, using the code GADGET-2 with unprecedentedly high spatial resolutions. The initial conditions for the cloud models are chosen to be the "standard isothermal test case" in the variant calculated by Burkert & Bodenheimer (1993) and the centrally condensed, Gaussian cloud advanced by Boss (1991). A barotropic equation of state is assumed to simulate the transition from isothermal to nonisothermal collapse. The first motivation of this study is to investigate the sensitivity of fragmentation to the effects of thermal retardation by varying the value of the critical density ($\rho_{\rm crit}$) at which nonisothermal heating is assumed to begin. The second goal is to explore the level of resolution needed by smoothed particle hydrodynamics (SPH) methods to achieve realistic fragmentation and convergence to existing Jeans-resolved, finite-difference (FD) calculations. Further reasons that justify the present study are (1) the complete lack of SPH calculations of the Gaussian-cloud collapse and (2) the fact that while a fairly good agreement exists that the outcome of the isothermal collapse of the Gaussian cloud is the formation of a singular filament, no definite solution has as yet been found for its barotropic collapse. The main results are summarized as follows.

The calculations show that increasing the number of particles from 0.6 to 1.2 million yields reasonable good convergence for the collapse and fragmentation of the standard isothermal test case. When $\rho_{\rm crit} = 5.0 \times 10^{-12}$ g cm^{-3}, the cloud fragments into a binary system connected by a thin filament, which never subfragments, in excellent agreement with previous adaptive FD

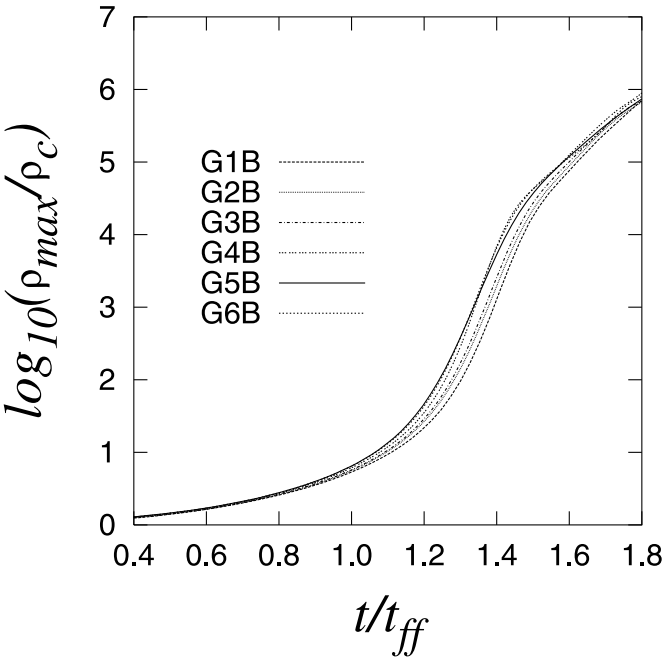

FIG. 14.—Time evolution of the maximum density for models G1B–G6B. The legend within the box specifies the model to which each curve corresponds.

calculations by Truelove et al. (1998) and SPH calculations by Kitsionas & Whitworth (2002). As long as the critical density is lowered to the value of 5.0×10^{-14} g cm^{-3}, which is more representative of the near isothermal phase (Boss et al. 2000), the cloud collapses to produce a binary core embedded in a circumbinary disk in much the same way as predicted by the adaptive FD calculations of Klein et al. (1999). In particular, the SPH calculations show that reasonably good convergence with Jeans-resolved, FD calculations is achieved for the collapse of the uniform cloud when the number of SPH particles is at least twice that demanded by the Jeans condition. For the uniform models, thermal retardation neither favors fragmentation nor increases the number of final fragments that form.

On the other hand, convergent results for the collapse of the Gaussian cloud are achieved only when working with 5–10 million particles. When $\rho_{\rm crit} = 5.0 \times 10^{-12}$ g cm^{-3}, the cloud collapses in a fashion similar to that predicted by the AMR calculations of Boss et al. (2000); that is, a single central core is formed surrounded by dense trailing spiral arms. When the GADGET-2 calculations are continued to peak densities higher than that reported by Boss et al. (2000), the spirals develop a clumpy structure, suggesting that fragmentation could eventually occur in the further evolution. Conversely, when the critical density is lowered to 5.0×10^{-14} g cm^{-3}, fragmentation into a quadruple system is seen to occur deep in the adiabatic collapse. In this case, fragmentation is quite similar to the "satellite" type fragmentation described by Matsumoto & Hanawa (2003) for the collapse of rapidly rotating, Bonnor-Ebert spheres. However, the quadruple system soon decays into a well-defined binary because of merging of the components of the quadruple core. Thus, the effects of thermal retardation result not only in fragmentation but also in an increase in the number of final fragments. While this result is at least valid for the early phases of collapse, leading to the formation of the first protostellar core, a definite answer to this question would demand continuing the calculations deeper into the evolution.

The reason for requiring about an order of magnitude more particles than demanded by the Jeans condition to ensure convergence for the Gaussian cloud compared to the uniform cloud is most probably due to intrinsic features of the SPH formalism implemented by GADGET-2. As was recently discovered by Attwood et al. (2007), the fidelity of adaptive SPH calculations of self-gravitating systems relies on requiring that the number of neighbors that contribute to the kernel volume be kept constant. In this way, nonlinear numerical dissipation and diffusion can be maintained at a low rate. In GADGET-2 the mass contained in the kernel volume, rather than the number of neighbors, is maintained constant. Therefore, if all particles share the same mass, as for the uniform-cloud models, the condition of constant mass is equivalent to having a constant number of neighbors. This explains why for the uniform models convergence is always attained at resolutions equal to or twice that demanded by the Jeans condition. Conversely, for the Gaussian-cloud models the SPH particles have unequal masses, in which case the condition of constant mass does not necessarily imply a constant number of neighbors. Convergence would then demand having a much larger total number of particles in order to significantly reduce the rates of numerical dissipation and diffusion. For the particular case of the Gaussian cloud, we find that GADGET-2 produces reliable results only when working with more than 5 million particles, corresponding to an order-of-magnitude more particles than demanded by the Jeans condition.

The calculations of this paper were performed using the computational facilities of the University of Sonora (Mexico). This work is partially supported by the Mexican Consejo Nacional de Ciencia y Tecnología (CONACyT) under contract U43534-R, the Fondo Nacional de Ciencia, Tecnología, e Innovación (Fonacit) of Venezuela under contract 200400103, the Deutsche Forshungsgemainshaft (DFG), and the Deutscher Akademischer Austauschdienst (DAAD). We thank Ricardo Duarte for helping us with the use of the graphics package PV-WAVE, and we thank the anonymous referee for providing a number of comments and suggestions that have improved the content and quality of the manuscript.

REFERENCES

André, P., Bacmann, A., Motte, F., & Ward-Thompson, D. 1998, in The Physics and Chemistry of the Interstellar Medium, ed. V. Ossenkopf, J. Stutzki, & G. Winnewisser (Zermatt: GCA-Verlag), 241
Anglada, G., Rodríguez, L. F., Osorio, M., Torrelles, J. M., Estalella, R., Beltrán, M. T., & Ho, P. T. P. 2004, ApJ, 605, L137
Attwood, R. E., Goodwin, S. P., & Whitworth, A. P. 2007, A&A, 464, 447
Basu, S., & Mouschovias, T. Ch. 1994, ApJ, 432, 720
Bate, M. R., & Burkert, A. 1997, MNRAS, 288, 1060
Boden, A. F., et al. 2005, ApJ, 635, 442
Bodenheimer, P. 1995, ARA&A, 33, 199
Bodenheimer, P., Burkert, A., Klein, R. I., & Boss, A. P. 2000, in Protostars and Planets IV, ed. V. Mannings, A. P. Boss, & S. S. Russell (Tucson: Univ. Arizona Press), 675
Boss, A. P. 1991, Nature, 351, 298
Boss, A. P. 1998, ApJ, 501, L77
Boss, A. P., & Bodenheimer, P. 1979, ApJ, 234, 289
Boss, A. P., Fisher, R. T., Klein, R. I., & McKee, C. F. 2000, ApJ, 528, 325
Boss, A. P., & Myhill, E. A. 1992, ApJS, 83, 311
Brandeker, A., Jayawardhana, R., & Najita, J. 2003, AJ, 126, 2009
Burkert, A., & Bodenheimer, P. 1993, MNRAS, 264, 798
———. 1996, MNRAS, 280, 1190
Ciolek, G. E., & Mouschovias, T. Ch. 1994, ApJ, 425, 142
Cutispoto, G., Pastori, L., Pasquini, L., de Madeiros, J. R., Tagliaferri, G., & Andersen, J. 2002, A&A, 384, 491
Duchêne, G., Bouvier, J., Bontemps, S., André, P., & Motte, F. 2004, A&A, 427, 651

Duquennoy, A., & Mayor, M. 1991, A&A, 248, 485
Fischer, D. A., & Marcy, G. W. 1992, ApJ, 396, 178
Ghez, A. M., McCarthy, D. W., Patience, J. L., & Beck, T. L. 1997, ApJ, 481, 378
Girart, J. M., Curiel, S., Rodríguez, L. F., Honda, M., Cantó, J., Okamoto, Y. K., & Sako, S. 2004, AJ, 127, 2969
Hennebelle, P., Whitworth, A. P., Cha, S.-H., & Goodwin, S. P. 2004, MNRAS, 348, 687
Hubber, D. A., Goodwin, S. P., & Whitworth, A. P. 2006, A&A, 450, 881
Hubrig, S., Le Mignant, D., North, P., & Krautter, J. 2001, A&A, 372, 152
Inutsuka, S.-I., & Miyama, S. M. 1992, ApJ, 388, 392
———. 1997, ApJ, 480, 681
Kitsionas, S., & Whitworth, A. P. 2002, MNRAS, 330, 129
Klein, R. I., Fisher, R. T., McKee, C. F., & Truelove, J. K. 1999, in Numerical Astrophysics 1998, ed. S. Miyama, K. Tomisaka, & T. Hanawa (Dordrecht: Kluwer), 131
Köhler, R., Kunkel, M., Leinert, C. H., & Zinnecker, H. 2000, A&A, 356, 541
Köhler, R., & Leinert, C. H. 1998, A&A, 331, 977
Leinert, C. H., Henry, T., Glindemann, A., & McCarthy, D. W. 1997, A&A, 325, 159
Looney, L. W., Mundy, L. G., & Welch, W. J. 1997, ApJ, 484, L157
———. 2000, ApJ, 529, 477
Masunaga, H., & Inutsuka, S.-I. 1999, ApJ, 510, 822
Masunaga, H., Miyama, S. M., & Inutsuka, S.-I. 1998, ApJ, 495, 346
Mathieu, R. 1994, ARA&A, 32, 465
Matsumoto, T., & Hanawa, T. 2003, ApJ, 595, 913
Monaghan, J. J. 1997, J. Comput. Phys., 136, 298
———. 2005, Rep. Prog. Phys., 68, 1703
Monaghan, J. J., & Lattanzio, J. C. 1985, A&A, 149, 135
Moriarty-Schieven, G. H., Powers, J. A., Butner, H. M., Wannier, P. G., & Keene, J. 2000, ApJ, 533, L143
Motte, F., André, P., & Neri, R. 1998, A&A, 336, 150
Mouschovias, T. Ch., & Ciolek, G. 1999, in The Origin of Stars and Planetary Systems, ed. C. J. Lada & N. Kylafis (NATO ASI Ser. C, 540; Dordrecht: Kluwer), 305
Patience, J. L., Ghez, A. M., Reid, I. N., Weinberger, A. J., & Matthews, K. 1998, AJ, 115, 1972
Reipurth, B., Rodríguez, L. F., Anglada, G., & Bally, J. 2002, AJ, 124, 1045
Sigalotti, L. Di G., & Klapp, J. 2001a, Int. J. Mod. Phys. D, 10, 115
———. 2001b, A&A, 378, 165
———. 2001c, in Exact Solutions and Scalar Field in Gravity: Recent Developments, ed. A. Macias, J. Cervantes, & K. Laemmerzhal (Dordrecht: Kluwer), 223
Springel, V. 2005, MNRAS, 364, 1105
Terebey, S., van Buren, D., Padgett, D. L., Hancock, T., & Brundage, M. 1998, ApJ, 507, L71
Truelove, J. K., Klein, R. I., McKee, C. F., Holliman, J. H., Howell, L. H., & Greenough, J. A. 1997, ApJ, 489, L179
Truelove, J. K., Klein, R. I., McKee, C. F., Holliman, J. H., Howell, L. H., Greenough, J. A., & Woods, D. T. 1998, ApJ, 495, 821
Tsai, J., & Bertschinger, E. 1989, BAAS, 21, 1089
Ward-Thompson, D., Scott, P. F., Hills, R. E., & André, P. 1994, MNRAS, 268, 276
Whitworth, A. P. 1998, MNRAS, 296, 442
Winkler, K.-H. A., & Newman, M. J. 1980, ApJ, 238, 311
Woitas, J., Leinert, Ch., & Köhler, R. 2001, A&A, 376, 982